The anatomy of exhumed river-channel belts: Bedform- to belt-scale river kinematics of the Cretaceous Cedar Mountain Formation, Utah, USA

Benjamin T. Cardenas[1,2]*, David Mohrig[1], Timothy A. Goudge[1], Cory M. Hughes[3], Joseph S. Levy[4], Travis Swanson[5], Jasmine Mason[1], and Feifei Zhao[1]

[1]Jackson School of Geosciences, University of Texas at Austin, Austin, TX, USA

[2]now at the Division for Geological and Planetary Sciences, California Institute of Technology, Pasadena, CA, USA

[3]Department of Geology, Western Washington University, Bellingham, WA, USA

[4]Department of Geology, Colgate University, Hamilton, NY, USA

[5]Department of Geology and Geography, Georgia Southern University, Statesboro, GA, USA

*Corresponding Author Contact Information

Telephone: (210) 240-0382

Email: bencard@caltech.edu

Re-submitted to Sedimentology after 1 round of revisions

THIS MANUSCRIPT IS IN REVISION AT SEDIMENTOLOGY AND HAS NOT COMPLETED THE PEER REVIEW PROCESS

Word Count: 96+7,759 (Title, authors, affiliations, main text except refs & captions, 8,000 limit)

Abstract: 256 (300 word limit)

Figures: 20

References: 109

ABSTRACT

Interpretations of fluvial depositional settings often require observations of facies changes over long distances or thick successions, which are not available everywhere. This work tests the hypothesis that a regional understanding of paleoriver kinematics, depositional setting, and sedimentation rates can be interpreted from local sedimentological measurements of bedform and barform strata. In the Ruby Ranch Member of the Cretaceous Cedar Mountain Formation, Utah, USA, bars, channel planform geometry, and bed topography are measured within exhumed fluvial strata exposed as ridges. The studied ridges are composed of stacked channel belts, representing at least 5 or 6 reoccupations of a single strand channel altogether. Lateral sections reveal well-preserved barforms constructed of subaqueous dune cross sets. The topography of paleobarforms is preserved along the top surface of the outcrop. Comparisons of the channel-belt centerline to local paleotransport directions, a measurement defined as the paleotransport anomaly, indicate channel planform geometry was preserved through the re-occupations, rather than being obscured by lateral migration. Rapid avulsions preserved the state of the active channel bed and its individual bars at the time of abandonment. Calculated minimum sedimentation durations for the preserved elements, inferred from cross-set thickness distributions and assumed bedform migration rates, vary within a belt from a day to 10 days. Using only these local sedimentological measurements, the depositional setting is interpreted as a fluvial megafan, given the similarity in river kinematics. This work provides a baseline and new techniques for the future synthesis of vertical and planview data, including the drone-equipped 2020 Mars Rover mission to exhumed fluvial and deltaic strata.

Keywords: fluvial sedimentology, channel belt, preservation, bar, sinuous ridge

INTRODUCTION

Fluvial channel belts are the total accumulation of a river's channel deposits over time. These channel deposits include strata associated with bedforms, such as ripples and dunes, as well bars, which may or may not be composed of ripples and dunes (Reesink and Bridge, 2011). The lateral migration, aggradation, and degradation of a river is recorded within the accumulations and bounding surfaces of these bedforms and bars, which in turn shape the resultant channel belts (Van De Lagewag et al., 2013). Therefore, in order to determine how ancient rivers migrated, aggraded, and avulsed, it is necessary to understand the accumulation and preservation of the bedform and barform strata within the associated channel belts (e.g., Reesink et al., 2015; Durkin et al., 2018; Paola et al., 2018; Chamberlin and Hajek, 2019). Furthermore, properties such as water and sediment discharge associated with an ancient fluvial system can only be accurately estimated using properties of its paleochannels, if these geometries can be accurately estimated from channel belts (Wright and Parker, 2003; Parker et al., 2007; Hayden et al., 2019).

This work examines an exhumed complex of fluvial deposits in the Ruby Ranch Member of the Cretaceous Cedar Mountain Formation, Utah, USA (Fig. 1). The goal is to test the hypothesis that local sedimentological measurements of dune and bar strata can be used to extract the regional kinematics and depositional setting of the formative rivers. Here, new methodologies utilizing quantitative field measurements are developed for extracting river-channel kinematics from channel-belt deposits. The measurements presented here cover the channel belts across a range of scales, from local stacks of cross sets to the entirety of the outcrop, in order to interpret the river systems of the Ruby Ranch Member. The datasets analyzed in this work include aerial images collected from a drone, field maps, vertical and lateral sections, modern river analogs, and another ancient example of fluvial stratigraphy in the nearby Jurassic Morrison Formation. Paleotransport-direction measurements collected from strata exposed on the top surfaces of exhumed channel-belts are compared to channel-belt outcrop centerlines to understand the degree of lateral migration recorded. The durations required to accumulate bar and thalweg strata are calculated using climb angles from cross-set thickness distributions and assumed bedform migration rates, and constrain timescales related to the vertical aggradation of channel belts. Preserved bar topography is identified by cross-set bounding surfaces that conform to the modern topography, and is relevant for understanding the types of avulsions these rivers experienced.

Background

Cedar Mountain Formation

The rivers that deposited the Ruby Ranch Member of the Lower Cretaceous Cedar Mountain Formation drained the uplifted Sevier thrust belt, in what is now modern-day western Utah, northeastward towards the Mowry Sea and its successor, the Western Interior Seaway (Currie, 1998, 2002). Ultimately, foreland-basin subsidence led to the burial of the Cedar Mountain Formation by late Cretaceous coastal and marine deposits of the Naturita

Formation (formerly the Dakota Sandstone; Young, 1960; Carpenter, 2014) and the Mancos Shale (Currie, 1998, 2002). A regional unconformity separates the base of the Cedar Mountain Formation from the top of the upper Jurassic Morrison Formation (Peterson and Ryder, 1975; Kowallis et al., 1986). The Cedar Mountain Formation has been interpreted as consisting of channel sandstones and conglomerates, and overbank mudstones and paleosols (Stokes, 1961; Currie, 1998; Garrison et al., 2007; Ludvigson et al., 2015; Nuse, 2015; Hayden et al., 2019).

The Cedar Mountain Formation is an important source of paleontological, climatic, and tectonic information (Heller and Paola, 1989; Currie, 1998, 2002; Kirkland et al., 1999; Ludvigson et al., 2010, 2015; Joeckel et al., 2019). Recent work regarding the Ruby Ranch Member of the Cedar Mountain Formation has focused on the geomorphology of exhumed channel deposits, which are more resistant than the surrounding floodplain material, resulting in the preferential erosion of floodplain strata and preservation of the channel deposits that form ridges (Williams et al., 2007; 2009; Hayden et al., 2019). These ridges are as tall as 35 m and 60-90 m wide on average, and expose channel deposits in three dimensions (Fig. 1). Recent interest in these landforms and other exhumed channel deposits (e.g., Hayden et al., 2019; in Oman, Maizels 1987, 1990; Maizels and McBean, 1990; in Egypt, Zaki et al., 2018) has partially been driven by high-resolution images of morphologically similar 'fluvial sinuous ridges' on Mars (e.g., Burr et al., 2009; Davis et al., 2016; Cardenas et al., 2018; Hughes et al., 2019). Hayden et al. (2019) have provided an important comparison between field- and remote-sensing-based paleohydraulic reconstructions for the exhumed channel deposits of the Cedar Mountain Formation, but the sedimentologic workup herein provides additional information for paleoenvironmental analysis.

Dune, bar, and channel belt strata

The dip direction of a dune cross stratum records the orientation of the formative dune lee face, and reflects local dune migration direction (Allen, 1970; Rubin and Hunter, 1982). This relationship is complicated for trough cross strata created by dunes with sinuous crestlines and variably deep troughs (McKee and Weir, 1953; DeCelles et al., 1983; Rubin, 1987). The local dip direction of a set of trough cross-stratification may represent the mean migration direction of the associated dune plus or minus as much as 90° (Dott Jr., 1973; Almeida et al., 2016). In plan-view exposures, the net migration direction can be determined reliably, as well as the orientation of the bar surface the dune migrated on (Dott Jr., 1973; Almeida et al., 2016). In channel deposits, larger dipping strata composed of smaller dune cross sets represent the accretion surfaces of barforms built by dunes (Allen, 1983; Edwards et al., 1983; Miall, 1985, 1988; Almeida et al., 2016).

Barforms are either fixed in position by channel shape or are free to migrate downstream, although these represent end members of a continuum (Miall, 1977; Seminara and Tubino, 1989; Ikeda, 1989; Hooke and Yorke, 2011). Bars fixed to the inner bank of a channel bend, called point bars, grow into the channel (Ikeda et al., 1981) and record lateral river migration. Point bars have been identified in the rock record based on sigmoidal lateral accretion surfaces dipping towards a range of orientations centered around approximately perpendicular angles to the local dip directions of dune cross strata (e.g., Edwards et al., 1983; Wu et al., 2015; Almeida et al., 2016). Free bars are able to migrate downstream, though they may be attached to banks, and preserve a wider array of relationships between local dune migration direction and the bar surface dip direction (e.g., Allen, 1983; Almeida et al., 2016). Free bars and point bars commonly coexist in channels and in mixed-case forms (Fig. 2) (Kinoshita and Miwa, 1974; Whiting and Dietrich, 1993; Hooke and Yorke, 2011). Both types of bar strata may therefore be observed in the Cedar Mountain Formation deposits.

In net-depositional settings, aggradation of the riverbed is coupled with aggradation of the channel margins, and occurs more rapidly than in the distal floodplain (Pizzuto, 1987). Over time, the channel becomes elevated relative to the floodplain, and the difference between the two elevations defines the channel's superelevation. Past studies have shown that a superelevation of 60% of the flow depth appears to be a threshold for river avulsion (Mohrig et al., 2000), the process by which flow abandons a channel in favor of a lower topographic pathway (Heller and Paola, 1996; Mohrig et al., 2000; Hajek and Edmonds, 2014; Chadwick, 2020). Studies of both modern and ancient avulsive rivers suggest that rivers tend to return to previously abandoned channels that became attractors to flow following the aggradation of the adjacent floodplain (Heller and Paola, 1996; Reitz et al., 2010; Edmonds et al., 2016). Such systems leave behind channel-belt complexes, defined as sedimentary deposits composed of stacked channel-belts (Friend, 1979; Mohrig et al., 2000; Jones and Hajek, 2007; Cuevas Martínez et al., 2010; Chamberlin and Hajek, 2015; Hayden et al., 2019).

Modern-analog rivers

Two modern rivers representing end-member braided and meandering planforms are used in this study. The North Loup is a sand-bed braided river that has been used as a modern analog to ancient fluvial strata (Mohrig et al., 2000; Mahon and McElroy, 2018). A drone photomosaic collected by Swanson et al. (2018) was used that images a 760 m reach of the river in which downstream migrating bars and dunes, as well as the channel banks, are clearly identifiable. This represents a potentially reasonable analog to understand bar and bedform processes occurring in the formative channels of the Cedar Mountain Formation, as widths and depths are similar. The eastern and western ridges are 63 and 90 m wide on average. The North Loup River is 111 m wide in the studied reach, and ~1 – 1.5 m deep (Mohrig and Smith, 1996; Hayden et al., 2019). This study also uses analyzed bedforms and bars in the meandering Trinity River from a joined digital elevation model consisting of a subaerial airborne lidar survey and acoustic bathymetric surveys (Mason and Mohrig, 2018; 2019a and b; Mason, 2018). These datasets provide 32 river km to map dune crests on the river bed. Though deeper than the formative rivers of the Cedar Mountain Formation, the Trinity River is of a similar width (122 m on average), which is more significant for this study focusing on the steering of dunes by bars.

METHODS

Field measurements

Several datasets were acquired at two adjacent ridges that are erosional remnants from what is interpreted to have been a single, continuous ridge of the Cedar Mountain Formation (Fig. 1A and B). These ridges were selected because of the accessibility to their sidewall and planview exposures. Although northwest-southeast trending normal faults have been mapped in the region, none appear to intersect these ridges (Sable, 1956; Hayden et al., 2019). Aerial photosurveys, collected with a DJI Phantom 2 Vision Plus drone, imaged the top and side surfaces of both ridges with >75% along-path and side overlap in photos (Fig. 1C-D). Flights were conducted at 15-20 m above ground level. Ground control point locations were determined using an Archer Field PC with an external GPS antenna, producing horizontal position data with <0.3 m RMS accuracy. Orthomosaics were generated with 5 cm spatial resolution using Agisoft Photoscan Pro (www.agisoft.com), and cover an area of 213,000 m^2 over the eastern and western ridges (Fig. 1C to D). These datasets were used to map the locations of bounding surfaces of cross-sets and major erosional surfaces. Dip directions of cross-strata identified on the photomosaics were measured in the field using compasses. Each set was classified as either being composed of sandstone or conglomerate.

Around the perimeters of each ridge, 59 vertical sections were measured covering the entirety of the available vertical exposure of the ridge-capping rock, resulting in 276 total meters of section. An additional 31 2-D panels ranging from 1 m to 10 m wide were collected around the perimeters of both ridges in order to describe the smaller, cross-set scale architectural elements of the channel belts. Architectural variability in the transport direction at the scale of a few meters was recorded, including changes in set thickness and the dips of bounding surfaces. Across all of these surveys, the thickness of 362 sets of cross strata were measured, and grain size was measured for 75 of those sets in the field using a SciOptic translucent grain-size chart. Using a geographic information system (GIS), field mapping results were merged with the remote sensing measurements. Ridge-scale bounding surfaces were digitized as lines, and 1,071 sets of planform-exposed trough cross strata and 107 exposures of large-scale dipping strata were digitized as polygons.

Transport anomaly

To test how well the ridge outcrop centerlines represent original channel centerlines, a new metric is developed and named here as the transport anomaly, Θ_{TA}. It is defined for both modern rivers and the exhumed channel deposits.

$$\Theta_{TA\text{-}CHANNEL} = \Theta_{CL\text{-}CHANNEL} - \Theta_{D\text{-}CHANNEL} \tag{1a}$$

$$\Theta_{TA\text{-}RIDGE} = \Theta_{CL\text{-}RIDGE} - \Theta_{D\text{-}RIDGE} \tag{1b}$$

where Θ_D is the 0 – 359° orientation of a transport or paleotransport measurement from an active dune ($\Theta_{D\text{-}CHANNEL}$; Eq. 1a) or cross set ($\Theta_{D\text{-}RIDGE}$; Eq. 1b), and Θ_{CL} is the orientation of the centerline nearest to the location where Θ_D was measured (Fig. 3). Values of Θ_{TA} may be positive or negative, and are calculated using the Circular Statistics Toolbox available for MATLAB, which measures the shortest angular distance, positive or negative, between the two directions such that no measurement exceeds 180° or is less than -180° (Berens, 2009).

By measuring $\Theta_{D\text{-}CHANNEL}$ from dunes in modern rivers and $\Theta_{TA\text{-}RIDGE}$ from planform-exposed cross sets in the Ruby Ranch Member of the Cedar Mountain Formation, hundreds of measurements of Θ_{TA} (Eq. 1a to b) between the ancient and modern systems were compared to test whether the transport anomalies for the outcrop are distinct from transport anomalies observed in a modern river system. To perform this comparison, Cedar Mountain Formation ridge centerline trends and paleotransports are required, as well as modern river centerlines and instantaneous transport directions collected from dune crest orientations. The braided North Loup River, Nebraska, USA, and the meandering Trinity River, Texas, USA, are used as the modern analogs.

This test was then used to understand how well the centerlines of the ancient rivers are preserved in the exhumed channel belts and represented by ridge geometry (Fig. 4A and B). For example, if the mean and standard deviation (σ) of $\Theta_{TA\text{-}RIDGE}$ *(Eq. 1b)* approximately equal those of $\Theta_{TA\text{-}CHANNEL}$ (Eq. 1a), then the transport anomaly of the ancient deposit is no greater than the variability in a modern river, and is consistent with channel-belt planform preserving the formative channel planform (Fig. 4A). If lateral migration and reworking has greatly widened the belt and reduced its overall sinuosity from that of the formative channels, σ should be greater in the ancient deposit, as well as a more random distribution of $\Theta_{TA\text{-RIDGE}}$ (Fig. 4B). An example of the latter case comes from point bar strata of the Ferron Sandstone in Wu et al., (2015, their Fig. 13; 2016, their Fig. 8), who present a general northwest-curving paleotransport trend along a northeast trending exposure, making their study location a high paleotransport anomaly zone. Furthermore, the deviation angle in Wu et al. (2016) is calculated relative to an interpreted channel-form, not the exhumed channel-belt shape. Wang and Bhattacharya (2017, their Fig. 10A) show an even clearer example linked to point bar growth. Durkin et al. (2018) show examples of this lateral amalgamation in ancient (McMurray Formation) and the modern (Mississippi and New Madrid Rivers). In a third scenario where erosion patterns have not exhumed the belt evenly from all directions, neither of the aforementioned scenarios would be observed.

Points defining the centerlines of rivers were calculated using the series of points defining each channel bank. For each point on one bank or ridge edge, the distance to the nearest point on the opposite bank or ridge edge is calculated and taken as a local width measurement, and a centerline point is placed at the location exactly between the two points. The sequence of points spanning the length of the ridges or a river reach was smoothed using a spline method in the MATLAB curve fitting toolbox. Centerlines are ultimately defined as points spaced ~1 m apart along the smoothed line.

To measure local transport directions in the analog rivers, the brink lines of modern dunes on the North Loup River bed were mapped using the orthorectified UAV photomosaic collected by Swanson et al. (2018). The orientation of each dune was estimated by a best-fit line to a series of mapped brink points. The normal to each brink line, in turn, was taken as the local transport direction for that dune, $\Theta_{D\text{-}CHANNEL}$. $\Theta_{D\text{-}CHANNEL}$ was then tied to a point located at the average XY coordinate of all XY coordinates defining that particular dune brink line. The same process was applied to bedforms over the 32 km reach of the Trinity River imaged using sonar profiles of dunes on the channel bed (dataset from Mason, 2018), as well as dunes frozen on subaerially exposed point bar surfaces formed during the previous bankfull flood imaged in a 2015 lidar survey (Mason and Mohrig, 2018; 2019b). The widths of these channels are comparable to the widths of the ridges, and the braided and meandering end-members are useful in interpreting the Cedar Mountain Formation, as the dominance of free bars in the former vs. point bars in the latter route flow in different ways (Dietrich & Smith, 1984; Ashworth, 1996). In the Cedar Mountain Formation, values for $\Theta_{D\text{-}RIDGE}$ are taken from field measurements of planform trough cross strata across the top surfaces of the two ridges and assigned associated XY coordinates at the center of the corresponding mapped set.

RESULTS

Vertical sections

The measured vertical sections from around the perimeters of each ridge were composed of over 99% cross-stratified sandstones and conglomerates. Where mudstones are incorporated within the vertical sections they are immediately below and scoured into by erosional surfaces that extend across ridges. Mudstone thickness can be up to 0.6 m thick and vary over meters-scale distances due to erosion from overlying channel elements. These persistent erosional surfaces commonly define and separate individual channel-belts (Fig. 5A and B and 6A and B; Friend et al., 1979). Any given vertical section exposes 1-4 stacked stories which locally vary in thickness from 0.10 m to 8.60 m, with a mean of 3.10 m ± 0.22 m (the calculated standard error of the mean), median of 2.80 m ± 0.27 m (the calculated standard error of the median) and σ of 2.03 m ± 0.15 m (the calculated standard error of the standard deviation; n = 89; Fig. 6C). These story-bounding surfaces are also exposed along the top surfaces of the ridges. Five of these surfaces have been mapped across the western ridge, and four have been mapped across the eastern ridge (Fig. 5C).

Sedimentary structures and architecture

The most common sedimentary structures preserved in planview and vertical exposures of the Cedar Mountain Formation ridges are trough cross sets (Fig. 7) with median grain sizes ranging from upper-fine sand to medium pebbles (Fig. 8A to C). The mean thickness of these sets is 0.12 m ± 0.005 m, with a standard deviation of 0.09 m ± 0.003 m, and a coefficient of variation of 0.79 ± 0.04 (c_v = σ/mean, with propagated errors; n = 350). Along the top ridge surfaces where these structures are exposed and mapped in planview (Fig. 9), the dominant dip direction of these sets was identified as representative of the associated bedform's migration direction. The polygons outlining these planform exposed sets (n = 1,071) sum to a total area of 5,019 m^2. Of the 1,071 sets mapped in planform, 269 were identified as conglomerate, representing 25.1% of sets and 26.5% (1,330 m^2) of total set area. The remaining 802 sets were identified as sandstone, representing 74.9% of sets and 73.5% (3,689 m^2) of total set area. Larger scale thicker compound cross-sets (n = 12), with a mean of 1.28 m ± 0.05 m and a σ of 0.19 m ± 0.04 m measured at preserved rollovers (topsets), are also exposed in planview (Fig. 10A-D). There was no overlap in thickness between the two structures. The locations of planview measurements of both types of sedimentary structures are shown in Figure 11. The summed planform exposure area of these sets (n = 103) is 520 m^2, or covering 10.3% of the planform area of trough cross-sets. Within individual channel belt stories, shingled trough cross-sets record transport up and down larger-scale topography (Fig. 12A-D).

Four arrangements of cross beds were observed (Figs. 13-14). Type A featured a thick basal set of compound strata scoured along its top by an upstream-dipping surface, and overlain by a thinner coset composed of smaller cross beds with a mean thickness and standard deviation of 0.12 m ± 0.01 m and 0.07 m ± 0.01 m (Fig. 13 and 14A-B). The upstream dips of the scour surface range from 5°-13° (mean = 7°, n = 6). In this case, orientation of small cross beds roughly parallel the dip direction of the larger cross beds.

Type B featured a thick basal set of compound cross-sets that change both dip and thickness in the downstream direction (Figs. 13 and 14C-D). Individual cross beds thickened by as much as 300% over the course of 1.5 meters in the downstream direction (0.08 m to 0.23 m, 0.07 m to 0.23 m, and 0.06 m to 0.19 m). Correspondingly, the bounding surfaces separating these cross beds shallow downstream from as steep as 26° to as shallow as 5°, and the upper bounding surface transitions from being markedly erosional to conformable. Similar to type A, the smaller cross beds roughly parallel the dip direction of the larger cross beds. The mean thickness and standard deviation of these sets at shallowly dipping sections was 0.13 m ± 0.01 m, and 0.08 m ± 0.01 m.

Type C was also composed of compound strata, but in these cases the dip directions of the smaller foresets were roughly transverse to the dip direction of the larger cross beds (Figs. 13 and 10D). Type C sets were mostly identified in plan-view exposures, so set thickness measurements were not made. Strata composing Types A, B, and C are sandstones.

Type D featured no compound cross-stratification, and bounding surfaces were sub-horizontal or showed local variable curvature associated with trough geometry (Figs. 13 and 14E-F). Type D strata featured pebble conglomerates and a ~ 90° scatter of transport directions, apparent by the juxtaposition of trough and dip-normal exposures . The mean thickness and σ of type D sets was 0.19 m ± 0.02 m and 14.7 m ± 0.02 m, and sections contain up to ten stacked sets.

Transport anomalies

Maps of transport anomalies (Θ_{TA}) for the Cedar Mountain Formation and North Loup River are presented in Fig. 15A to C. The associated Θ_{TA} histograms and statistical moments for these systems and the Trinity River are presented in Figure 16A to D. Significantly, all datasets have mean values ranging between -12 and +6 degrees, and standard deviations ranging from 25° to 35°. In the North Loup, anomalies were clearly controlled by local bar topography, but measurements approach the reach mean when assembled over a downstream distance of ~3 bar lengths, or half the reach length, indicating the variability is adequately sampled (Figs. 15C and 17A to C). In the Trinity, as expected for meandering rivers, both the magnitude of the mean and standard deviation of the transport anomalies are the smallest (Fig. 16D). Transport anomalies that are observed are located along point bar surfaces (Dietrich and Smith, 1984). In the Cedar Mountain, areas with concentrated high anomalies were found to be located at ridge bends with concentrations of transport-normal-dipping accretion surfaces (Fig. 15A to B).

DISCUSSION

Dune, bar, belt, and overbank strata

A distinction is drawn between cross sets on either side of the break in scale shown in Figure 8A. The thinner-bedded trough cross strata (Fig. 7) are interpreted as forming via the migration of 3-D dunes with variably deep troughs (Rubin, 1987). In planform and vertical sections, these are clearly distinct from larger-scale dipping strata (Fig. 10A to D), which do not show the same bounding-surface curvature and, significantly, feature cross strata defined by compound cross-sets (Figs. 10D and 14C to D). These larger-scale strata are interpreted as accretionary river-bar sets (Edwards et al., 1983; Haszeldine, 1983; Almeida et al., 2016). The population of dip direction vs. centerline trend anomalies for the bar strata feature a larger spread of values and modes situated far from zero (compare Fig. 16A to D against Fig. 16E to F). The range of values, particularly the dominance of paleoflow-normal values, suggests the formative bar types included point bars with primarily cross-stream accreting surfaces (Fig. 10D), and free bars which can feature cross-stream-, downstream-, and upstream-dipping accretion surfaces (Skelly et al., 2003; Almeida et al., 2016). Point bar structures are also interpreted from ridge-scale observations, where clusters of bar surfaces dip towards the convex sides of ridge bends (Fig. 11A to B; note that the western-most point bar strata define a convex-north bend, Fig. 1C). Free bars, discussed below, can be observed on a much smaller scale, and are represented by scattered bar accretion surfaces (Fig. 11A to B).

Together, these dune- and bar-scale cross strata are interpreted as channel belts formed during episodes of active sediment transport within that channel reach. The mudstones associated with ridge-scale erosional surfaces are interpreted to represent sedimentation during periods of channel abandonment, which indicates a system that experienced multiple avulsions and channel reoccupations (Mohrig et al., 2000; Jones and Hajek, 2007; Cuevas Martínez et al., 2010). The observed mudstone layers are laterally discontinuous, which we interpret as due to local scour associated with re-occupation that created the erosional surface. Thus, the ridges represent channel-belt complexes composed of stacked, individual channel belts, and the stratigraphic continuity between the two ridges suggests they once formed a continuous deposit.

The four cross-stratal types observed in the Cedar Mountain ridges document the interaction of the ancient dunes and bars in the formative river channels (Figs. 13 and 14). Type A architectures are characteristic of free bars, and possess a bar-scale bounding surface separating bar lee strata below from deposits of the bar stoss surface above (Fig. 14A to B). As such, this bounding surface preserves the characteristic dip of the stoss side of the bar form. The bar lee strata may be compound in that they are composed of dune cross sets, or bar slip faces, which may nonetheless be influenced by superimposed dunes and ripples (Reesink and Bridge, 2011; Reesink, 2018). At first glance, it might seem surprising to accumulate a coset of stoss-side deposits, but theory (Paola and Borgman, 1991) and a recent morphodynamic bedform model (Swanson et al., 2019) show that set stacking can occur even under conditions of net bypass or erosion because of variability in dune scour depths.

Type B architectures highlight change in compound dune strata due to migration of free bars (Figs. 13 and 14C to D). The steepest 26° cross strata represent bar lee construction most perpendicular to the average transport direction. The observed shallowing of bounding-surface dips and thickening of sets in the downstream direction records the planform deformation of the bar crest over time, where steep downstream-accreting surfaces gradually become more laterally accreting. As evident from the compound nature of these sets, this bar growth is driven by dune accretion in front of the bar. At the two locations where A and B type architectures are adjacent (Figs. 14A to D), the transition of the stoss scour surface to the conformable bounding surface of a cross-stratum represents the delivery of sediment mined from the bar stoss up and over the crest of the bar, and onto the bar lee. Taken together, these two architectures preserve the processes associated with bar migration via the mining and delivery of sediment by a surface veneer of smaller dunes compound to a larger free bar. We interpret these as the ‘form sets’ of compound bars (Reesink et al., 2015). One lateral section shows the stacking of lee strata on stoss strata, recording the aggradation and migration of a bar (Fig. 14G to H).

The type C compound strata define bar growth at an oblique angle to the net transport direction, and define the lateral migration of a bank-attached bar form (Fig. 10D). The coarser, non-compound type D architectures are interpreted as thalweg deposits (Fig. 14E to F). Together, these four architectural types describe the construction of channel-bottom topography within individual channel belts via the migration and growth of dunes (both on bars and in the thalweg), free bars, and point bars.

Channel-bed topography

Preserved bar form topography is interpreted to record the moment of channel abandonment (Fig. 12A to D). Two lines of evidence support this. First, in both cross section and map view, the compound relationship between dune and bar strata informs us that entire bar forms are preserved, complete with bar rollover (topset, Figs. 12, 13, 14, and 19). Second, the stoss-positioned dune sets are restricted to a surface veneer composing less than the upper 25% of the bar, with the remainder composed of steeply dipping bar-scale strata. If deflation of ridge surfaces commonly broke through the surface veneer of stoss dune sets, large bar scale strata would constitute a greater percentage of sedimentary structures exposed on ridge surfaces. Instead, dunes occupy an order of magnitude more surface area of the outcrop. The preservation of the river-bottom topography at the time of avulsion is interpreted to be the consequence of a relatively rapid channel abandonment coupled with minimal erosion of the channel deposit by the subsequent channel reoccupation.

Channel-planform geometry

The near zero means and the high kurtosis of the Cedar Mountain Formation paleotransport anomaly measurements, coupled with the similarity of the standard deviations measured in the ancient and the modern, are interpreted to indicate that the channel-belt-complex geometry preserves the formative river centerline in a reliable way (Fig. 16A to D). Regions of the channel belts showing concentrations of high transport anomaly measurements are associated with point bar lateral accretion surfaces (Figs. 1C, 11A to B, and 16A to B), supporting the hypothesis that lateral point bar migration is a cause of high anomaly measurements (Fig. 4B). However, these regions do not represent a majority of the ridge area.

The studied ridges are composed of several vertically stacked channel deposits. The preservation of the formative river channel centerlines through multiple re-occupations of the channel is expected in fluvial settings with high rates of vertical aggradation within the channel relative to lateral migration rates (Gibling, 2006; Jerolmack and Mohrig, 2007). As a result, there is a general lack of centerline distortion, even though the ridge represents a complex of stacked channel belts.

Channel-belt thickness

Because avulsions are likely to occur when a channel bed has aggraded to a sufficient level of superelevation, the thickness of a preserved channel belt, on average, is posited to equal paleochannel depth plus an aggradational component. The thickness of a free bar sets from topset to bottomset is assumed to be a measure of local channel depth (Mohrig et al., 2000). Bar measurements reported in Fig. 8A suggest an overall, mean channel depth of 1.28 ± 0.05 m. The mean belt thickness of 3.10 m ± 0.22 m (Fig. 6C) is then composed of an aggradational component consisting of 1.82 m ± 0.20 m. This indicates that, on average, a channel aggraded to a height of 1.53 ± 0.22 times its original depth before avulsing, creating a channel belt with a total thickness of 2.42 ± 0.19 times its flow depth.

River-bed kinematics

Dune accumulation on bars and in the thalweg

Analysis of Paola and Borgman (1991) shows that bedforms with gamma-distributed heights create a predictable exponential distribution of set thicknesses in cases of no net aggradation. Bridge and Best (1997) and Jerolmack and Mohrig (2005) emphasize the importance of bed aggradation as a control on the distribution of set thickness, showing that increased aggradation rates decrease the relative control of variable scour depth on set thickness. Jerolmack and Mohrig (2005) showed that the coefficient of variation (c_v) of set thicknesses decreases from a value of 0.88 in the case of no aggradation, to values approaching the c_v of the formative bedform heights with significant bed aggradation. Coupled with this change in c_v is a gradual shift from the predicted exponential distribution of set thicknesses, to a gamma distribution mirroring the distribution of the formative bedforms. Significantly, this analysis has been shown to be general enough to apply to ancient fluvial (Jerolmack and Mohrig, 2005) and aeolian strata (Swanson et al., 2019; Cardenas et al., 2019). Therefore, the reporting and analysis of set thickness distributions should be considered a significant part of any quantitative reconstruction of clastic sedimentary systems where there is an interest in understanding the kinematics and transport within the ancient system.

When taken together, all measured dune set thicknesses (n = 350) have a c_v of 0.79 ± 0.04 (Fig. 8A). This value implies set production by variable scour under conditions of minimal bed aggradation (c_v = 0.88 ± 0.03 for bypass case in Bridge 1997). The scour-dominated case also creates laterally discontinuous sets (Jerolmack and Mohrig, 2005; Cardenas et al., 2019). This scour dominance appears to be at odds with the preservation of bar 'form sets' described above (Figs. 14C to D). To understand the construction of the channel belt, measurements must be subdivided by environment and locally standardized to account for variability in bedform height at the reach scale, which is not necessarily representative of local variabillity (Reesink et al., 2015). Assembling all measurements into a single calculation without considering local architecture can result in inaccurate interpretations.

Set-thickness analysis performed separately for bar lee sets, bar stoss sets, and thalweg sets yields a different result then the bulk description. The first step in analyzing data from each sub-environment was to divide each set thickness by the mean set thickness for its local coset. These dimensionless values of set thickness were then collected for every bar lee, bar stoss, and thalweg deposit. Standardized cumulative distribution functions (CDFs) are shown in Figure 18. Coefficients of variation for the standardized distributions are 0.29 ± 0.04 for lee sets, 0.47 ± 0.07 for stoss sets, and 0.67 ± 0.10 for thalweg sets. Although c_v values as low as 0.29 were not examined by Jerolmack and Mohrig (2005), interpolation of their Figure 4B leads to a ratio of aggradation rate (*r*) to migration rate (*c*) for lee sets of ~ 10^{-1} (climb angle from 5°-6°). Stoss sets have r / c of ~$10^{-1.5}$ (climb angle from 1°-2°), and thalweg sets have r / c of ~$10^{-2.5}$ (climb angle from 0.1°-0.2°). The lee sides of downstream-migrating barforms, where the most sediment accumulation is expected (Reesink et al., 2015), have the highest ratio of aggradation rate to migration rate. This significant aggradation is supported by a Kolmogorov-Smirnov statistical test comparing the measurements to fitted exponential and gamma curves (Fig. 18A to C). For lee sets, the exponential curve is rejected at a significance level of 0.05 ($p < 0.001$), and the gamma curve is not ($p = 0.46$). This is consistent with the observed stacking and downstream thickening of sets in lee-type architectures (Fig. 14C to D). Even though thalweg sets are rejected as being exponentially distributed ($p = 0.02$) and not rejected as gamma distributed ($p = 0.17$), the two fitted curves are more similar than in the lee and stoss cases.

A non-trivial amount of climb is recorded by stoss sets, given the c_v of 0.47 ± 0.07, rejection of an exponential fit ($p = 0.01$), and non-rejection of a gamma fit ($p = 0.90$). This shows that the thin sets on the stoss side of the bar are not exclusively associated with erosion.

Deformation of the stoss side can drive aggradation of dune sets. Using ground-penetrating radar cross sections, Skelly et al. (2003) also interpreted upstream accretion in recent fluvial channel deposits of the Niobrara River, Nebraska, USA, which represent the growth and deformation of bars as they migrate.

Constraints on the time recorded by individual channel belts

How is time distributed through Cedar Mountain Formation channel belts? Backing out sedimentation rates from these strata would provide information on the kinematics of the formative rivers, as well as how local controls might dictate the construction of the rock record (Sadler, 1981; Jerolmack and Sadler, 2015; Paola et al., 2018). The distribution of cross-set thicknesses, in conjunction with assumed bedform migration rates, can provide some sense of the minimum amount of time associated with aggradation of each channel belt. This analysis is performed for the two major channel belt components observed here, bar and thalweg accumulations.

Given that the accumulation of dune sets at the bar lee is the process through which these bars migrated (Fig. 14C to D), it follows that

$$r_{lee} / c_{lee} = s_{bar} / m_{bar} \qquad (2)$$

where r_{lee} is the aggradation rate of the bed, c_{lee} is the migration rate of dunes, r_{lee} / c_{lee} of bar lee sets is calculated in the prior section as 10^{-1}, and s_{bar} / m_{bar} is the bar thickness over the equivalent migration distance (Fig. 19). Solving for m_{bar}, the only unknown, yields 12.8 m ± 0.5

m of bar migration, with uncertainty based on the number of measurements. Downstream-migrating bars migrate ~10 m per day in the North Loup and other rivers (Meade, 1985; Mohrig and Smith, 1996). Assuming this is a comparable rate to the ancient Cedar Mountain Formation fluvial system, which is a reasonable, order of magnitude assumption given the similar flow depths, channel widths, and the distribution of dune heights in the North Loup relative to our measured cross-set thicknesses (Mohrig and Smith, 1996), the observed lee architectures are a record of only ~1.28 ± 0.05 days of sedimentation. This suggests the bar strata and associated compound dune strata do not record the gradual aggradation of the channel bed leading up to avulsion, but rather record the higher frequency modification of the channel bed via bar migration. That is, net bed aggradation was not driven by bar climb. Instead, it is hypothesized that the aggradation of the channel bed is recorded in thalweg strata. This is supported by the clear distinction between thalweg and bar lee facies (Fig. 14E to F), which may not exist if bed aggradation was driven by climbing bars. To further test this hypothesis, Equation 2 is redefined in terms of the thalweg sets and the average thickness of the aggradational component of the channel belts, with a slower aggradation rate predicted. Assuming steady construction at North Loup dune migration rates (~60 m per day, Mohrig and Smith, 1996), only 9.7 days ± 1.1 days are required to accumulate the thalweg strata reported here. While indeed longer-term accumulations than the bar strata, these sets do not record slow channel aggradation over avulsion timescales.

For most rivers, occupation may last anywhere from years to thousands of years (Stouthamer and Berendsen, 2001; Slingerland and Smith, 2004). It is unlikely these channels were only occupied for 9.7 days. Instead, these strata may only represent the aggradation that occurred during the final episode of sedimentation that preceded avulsion and channel abandonment. This episode is likely to coincide with the final flood prior to avulsion. This result suggests that the channel was in a state of bypass for most of its occupation. Had channel abandonment not prevented it, the aggradation recorded by each channel belt would likely have been completely reworked (Fig. 20). The complete reworking of the channel bed during flood stage has been observed in modern net-depositional rivers (Nittrouer et al., 2011a) and in experiments (Leary and Ganti, 2020). This also suggests that floodplain deposits might more completely record successive episodes of flood-stage deposition than channel deposits, as presumably an episode of floodplain deposition is not immediately followed by reworking and removal.

Channel vs. floodplain accumulation

On average, a formative river of the Ruby Ranch Member of the Cedar Mountain Formation constructed a channel belt that was 2.42 ± 0.19 times thicker than its characteristic flow depth before avulsing. This thickness to depth ratio is somewhat larger than the value of 1.84 measured for the ancient Guadalope-Matarranya fluvial system in Spain (Mohrig et al., 2000; their Table 2). Without preserved levee deposits, it is unclear whether the increased relative belt thickness recorded by the Ruby Ranch Member is connected to an increase in incision depth or channel superelevation. However, the preservation of mudstones between vertically stacked channel belts, as well as preserved bar rollovers suggest that the standardized incision depths for the Ruby Ridge were comparable to the Guadalope-Matarranya system

(Mohrig et al., 2000). Assuming that the threshold superelevation trigger for avulsion proposed by Mohrig et al. (2000) is suitably general, the increased bed aggradation for Ruby Ridge channel belts is hypothesized to have required increased Ruby Ridge floodplain aggradation compared to the Guadalope-Matarranya system. That is, in order for the channel bed to reach the threshold superelevation to avulse, more channel bed aggradation was required during the final depositional episode to catch up with levees and floodplain that steadily aggraded during each bankfull event (Fig. 20). This scenario is consistent with the interpreted reworking of the channel bed between bankfull events, where any associated accumulation and scouring are reworked or filled such that there is no net channel bed change shortly after. This is contrasted by steady, gradual levee and floodplain aggradation, assuming these overbank environments are less likely to be reworked between floods.

Large-scale depositional setting

The interpreted kinematics of the Cedar Mountain Formation rivers are consistent with the kinematics reported for megafan channels. Channels in Andean megafans are highly unstable and mobile, and avulse on the scale of years, limiting any significant lateral migration (e.g., Horton and DeCelles, 2001; Chakraborty et al., 2010). Broader channel belts can develop on megafans, but these are generally limited to meandering rivers confined within lobe-cutting incised valleys that prevent avulsions (Assine et al., 2014). We therefore interpret the Ruby Ranch Member of the Cedar Mountain Formation to represent the accumulations of an early Cretaceous megafan or megafans draining the Sevier orogenic belt. Given the importance of floodplain aggradation in stacking these channel belts, the Ruby Ranch Member likely represents a medial fan setting (Owen et al., 2015). This contribution is useful in that a regional interpretation of depositional setting can be made using only local sedimentology, possibly even in cores, without the dependence on observing fan-scale changes in facies which may not be exposed well enough in all formations (e.g., Owen et al., 2015).

CONCLUSIONS

Ridges of the Ruby Ranch Member of the Cretaceous Cedar Mountain Formation are channel-belt complexes, composed of five or six stacked channel belts. Each channel belt is composed of bar and dune strata in a variety of compound relationships indicating the role of the latter in the accumulation of the former. Specifically, bars created topography, which forced dune sedimentation in the space in front of the bar, driving further bar migration.

Free-bar migration rates are estimated from thickness distributions of compound dune cross strata. Free bars represent only about 1 day of accumulation, yet represent on average 41% of a channel belt’s total thickness. Thalweg dune accumulations represent the rest of the belt and the aggradation of the channel bed, and are distinct from bar strata; bar climb did not aggrade the channel bed. Thalweg cross-set-thickness distributions are used to calculate the duration of bed aggradation at only about 10 days. These 10 days are interpreted to represent the final bankfull episode preceding avulsion, rather than the duration of the entire occupation of the channel. Prior bankfull accumulations that did not lead to avulsion were reworked to their original elevation by normal flows. Therefore, these channels primarily functioned as conduits for bypassing sediment, and most of the total time recorded by these channel belts is represented by its basal erosional surface.

Two aspects of the formative river systems are preserved particularly well, and record frequent and rapid avulsions, and a minor amount of total lateral migration. First, free bars are preserved completely, from stoss to lee, and are observed in both vertical sections and as topography on ridge tops. This is significant on its own; if this paleobar topography can be detected using remote sensing, future work could use it to better constrain flow depths of ancient rivers from fluvial channel belts exposed at the surface of Mars. Second, the planform geometry of the ridge and channel-belt complex represents the planform geometry of the formative rivers well, despite multiple reoccupations. Frequent, rapid avulsions and limited lateral migration are consistent with megafan channels, thus we interpret a megafan as the depositional setting of these channel-belt complexes. This provides a way to interpret regional depositional setting using the local sedimentology, rather than requiring regional exposure showing predicted facies changes.

Significantly, the synthesis of vertical and planform channel belts measurements shown here can provide a baseline for future studies facilitated by high resolution, drone-derived planform datasets. This may be particularly useful for the upcoming 2020 Mars Rover mission to Jezero crater, which will examine exhumed fluvial and deltaic strata using rover-mounted cameras and the first drone on Mars.

ACKNOWLEDGEMENTS

We thank Chief Editor Ian Kane, Associate Editor Christopher Fielding, Arjan Reesink, Matt Joeckel, and two anonymous reviewers for constructive feedback that helped improve this manuscript. Hima Hassenruck-Gudipati, Woong Mo Koo, and David Brown are thanked for their field assistance. The staff of Green River State Park, Utah, were accommodating to our large group. This work has improved following discussions with members of the David Mohrig Research Group and the Quantitative Clastics Laboratory, as well as Wonsuck Kim, Joel Johnson, Zoltan Sylvester, Cole Speed, Paola Passalacqua, Alistair Hayden, Mike Lamb, Becky Williams, Jenn Pickering, and Tim Demko. Funding was provided by the University of Texas Jackson School of Geosciences, the University of Texas Graduate School, and the RioMAR Industry Consortium.

DATA AVAILABILITY

The data that support the findings of this study are available from the corresponding author upon reasonable request.

REFERENCES

Allen, J.R.L. (1970) A Quantitative Model of Climbing Ripples and Their Cross-Laminated Deposits. *Sedimentology*, **14**, 5–26.

Allen, J.R.L. (1983) Studies in fluviatile sedimentation: bars, bar-complexes and sandstone sheets (low-sinuosity braided streams) in the Brownstones (L. Devonian), Welsh Borders. *Sedimentary Geology*, **33**, 237–293.

Almeida, R.P., Freitas, B.T., Turra, B.B., Figueiredo, F.T., Marconato, A., and **Janikian, L.** (2016) Reconstructing fluvial bar surfaces from compound cross-strata and the interpretation of bar accretion direction in large river deposits. *Sedimentology*, **63**, 609–628.

Ashworth, P.J. (1996) Mid-channel bar growth and its relationship to local flow strength and direction. *Earth Surface Processes and Landforms*, **21**, 103-123.

Assine, M.L., Corradini, F.B., Pupim, F. do N., and **McGlue, M.M.** (2014) Channel arrangements and depositional styles in the São Lourenço fluvial megafan, Brazilian Pantanal wetland. *Sedimentary Geology*, **301**, 172-184.

Berens, P. (2009) CircStat: A MATLAB Toolbox for Circular Statistics. *Journal of Statistical Software*, **31**, 1-21.

Bridge, J.S. (1997) Thickness of sets of cross strata and planar strata as a function of formative bed-wave geometry and migration, and aggradation rate. *Geology*, **25**, 971-974.

Bridge, J.S., and **Best, J. (1997)** Preservation of planar laminae due to migration of low-relief bed waves over aggrading upper-stage plane beds: comparison of experimental data with theory. *Sedimentology*, **44**, 253-262.

Burr, D.M., Enga, M.-T., Williams, R.M., Zimbelman, J.R., Howard, A.D., and **Brennand, T.A.** (2009) Pervasive aqueous paleoflow features in the Aeolis/Zephyria Plana region, Mars. *Icarus,* **200**, 52-76.

Cardenas, B.T., Mohrig, D., and **Goudge, T.A.** (2018) Fluvial stratigraphy of valley fills at Aeolis Dorsa, Mars: Evidence for base-level fluctuations controlled by a downstream water body. *Geological Society of America Bulletin*, **130**, 484-498.

Cardenas, B.T., Kocurek, G., Mohrig, D., Swanson, T., Hughes, C.M., and **Brothers, S.C.** (2019) Preservation of autogenic processes and allogenic forcings within set-scale aeolian architecture II: the scour-and-fill dominated Jurassic Page Sandstone, Arizona, USA. *Journal of Sedimentary Research***, 89**, 741-760.

Cardenas, B.T., Swartz, J.M., Mohrig, D., Prokocki, E.W. Setting up the preservation of fluvial channel belts. *Geology*, in review.

Carling, P.A., and **Leclair, S.F.** (2019) Alluvial stratification styles in a large, flash-flood influenced dryland river: The Luni River, Thar Desert, north-west India. *Sedimentology*, **66**, 102-128.

Carpenter, K. (2014) Where the sea meets the land: the unresolved Dakota problem in Utah. *Utah Geological Association Publication*, **43**, 357-372.

Chadwick, A.J. (2020) Mechanics of river avulsions on lowland river deltas. *PhD Dissertation, California Institute of Technology*, https://doi.org/10.1029/2019GL082491.

Chakraborty, T., Kar, R., Ghosh, P., and **Basu, S.** (2010) Kosi megafan: Historical records, geomorphology and the recent avulsion of the Kosi River. *Quaternary International*, **227**, 143-160.

Chamberlin, E.P., and **Hajek, E.A.** (2015) Interpreting paleo-avulsion dynamics from multistory sand bodies. *Journal of Sedimentary Research*, **85**, 82–94.

Chamberlin, E.P., and **Hajek, E.A.** (2019) Using bar preservation to constrain reworking in channel-dominated fluvial stratigraphy. *Geology*, **47**, 531-534.

Cuevas Martínez, J.L., Cabrera Pérez, L., Marcuello, A., Arbués Cazo, P., Marzo Carpio, M., and **Bellmunt, F.** (2010) Exhumed channel sandstone networks within fluvial fan deposits from the Oligo-Miocene Caspe Formation, South-east Ebro Basin (North-east Spain). *Sedimentology*, **57**, 162–189.

Currie, B.S. (1998) Upper Jurassic-Lower Cretaceous Morrison and Cedar Mountain Formations, Ne Utah-NW Colorado: Relationships between Nonmarine Deposition and Early Cordilleran Foreland-Basin Development. *Journal of Sedimentary Research*, **68**, 632-652.

Currie, B.S. (2002) Structural configuration of the Early Cretaceous cordilleran foreland-basin system and the Sevier thrust belt, Utah and Colorado. *The Journal of Geology*, **110**, 697-718.

Davis, J.M., Balme, M., Grindrod, P.M., Williams, R.M.E., and **Gupta, S.** (2016) Extensive Noachian fluvial systems in Arabia Terra: implications for early Martian climate. *Geology*, **44**, 847-850.

DeCelles, P.G., Langford, R.P., and **Schwartz, R.K.** (1983) Two New Methods of Paleocurrent Determination from Trough Cross-Stratification. *Journal of Sedimentary Research*, **53**, 629-642.

Dietrich, W.E., and **Smith, J.D.** (1984) Bed load transport in a river meander. *Water Resources Research*, **20,** 1355-1380.

Dott, R.H., Jr. (1973) Paleocurrent Analysis of Trough Cross Stratification. *Journal of Sedimentary Research*, **43**, 779-783.

Durkin, P.R., Hubbard, S.M., Holbrook, J., and **Boyd, R.** (2018) Evolution of fluvial meander-belt deposits and implications for the completeness of the stratigraphic record. *Geological Society of America Bulletin,* **130**, 721-739.

Edmonds, D.A., Hajek, E.A., Downton, N., and **Bryk, A.B.** (2016) Avulsion flow-path selection on rivers in foreland basins. *Geology*, **44**, 695–698.

Edwards, M.B., Eriksson, K.A., and **Kier, R.S.** (1983) Paleochannel geometry and flow patterns determined from exhumed Permian point bars in north-central Texas. *Journal of Sedimentary Research*, **53**, 1261-1270.

Friend, P.F., Slater, M.J., and **Williams, R.C.** (1979) Vertical and lateral building of river sandstone bodies, Ebro Basin, Spain. *Journal of the Geological Society*, **136**, 39–46.

Ganti, V., Paola, C., and **Foufoula-Georgiou, E.** (2013) Kinematic controls on the geometry of the preserved cross sets. *Journal of Geophysical Research: Earth Surface,* **118**, 1296-1307.

Garrison, J.R., Brinkman, D., Nichols, D.J., Layer, P., Burge, D., and **Thayn, D.** (2007) A multidisciplinary study of the Lower Cretaceous Cedar Mountain Formation, Mussentuchit Wash, Utah: a determination of the paleoenvironment and paleoecology of the Eolambia caroljonesa dinosaur quarry. *Cretaceous Research*, **28**, 461–494.

Gibling, M.R. (2006) Width and thickness of fluvial channel bodies and valley fills in the geological record: a literature compilation and classification. *Journal of Sedimentary Research*, **76**, 731–770.

Goudge, T.A., Mohrig, D., Cardenas, B.T., Hughes, C.M., and **Fassett, C.I.** (2018) Stratigraphy and paleohydrology of delta channel deposits, Jezero crater, Mars. *Icarus*, **301**, 58–75.

Hajek, E.A., and **Edmonds, D.A.** (2014) Is river avulsion style controlled by floodplain morphodynamics? *Geology*, **42**, 199-202.

Hartley, A.J., Owen, A., Swan, A., Weissmann, G.S., Holzweber, B.I., Howell, J., Nichols, G., and **Scuderi, L.** (2015) Recognition and importance of amalgamated sandy meander belts in the continental record. *Geology*, **43**, 679-682.

Hayden, A.T., Lamb, M.P., Fischer, W.W., Ewing, R.C., McElroy, B.J., and **Williams, R.M.E.** (2019) Formation of sinuous ridges by inversion of river-channel belts in Utah, USA, with implications for Mars. *Icarus*, **332**, 91-110.

Heller, P.L., and **Paola, C.** (1989) The paradox of Lower Cretaceous gravels and the initiation of thrusting in the Sevier orogenic belt, United States Western Interior. *Geological Society of America Bulletin*, **101**, 864-875.

Heller, P.L., and **Paola, C.** (1996) Downstream changes in alluvial architecture: an exploration of controls on channel-stacking patterns. *Journal of Sedimentary Research*, **66**, 297-306.

Hooke, J.M., and **Yorke, L.** (2011) Channel bar dynamics on multi-decadal timescales in an active meandering bar. *Earth Surface Processes and Landforms*, **36**, 1910-1928.

Hughes, C.M., Cardenas, B.T., Goudge, T.A., and **Mohrig, D.** (2019) Deltaic deposits indicative of a paleo-coastline at Aeolis Dorsa, Mars. *Icarus*, **317**, 442-453.

Ikeda, H. (1989) Sedimentary controls on channel migration and origin of point bars in sand-bedded meandering rivers. In S. Ikeda and G. Parker (Eds.), River Meandering: Water Resources Monograph, **12**, 51-68. American Geophysical Union: Washington, D.C.

Ikeda, S., Parker, G., and **Sawai, K.** (1981) Bend theory of river meanders. Part 1. Linear development. *Journal of Fluid Mechanics*, **112**, 363-377.

Jerolmack, D.J., and **Mohrig, D.** (2005) Frozen dynamics of migrating bedforms. *Geology*, **33**, 57-60.

Jerolmack, D.J., and **Mohrig, D.** (2007) Conditions for branching in depositional rivers. *Geology*, **35**, 463–466.

Joeckel, R.M., Ludvigson, G.A., Möller, A., Hotton, C.L., Suarez, M.B., Suarez, C.A., Sames, B., Kirkland, J.I., and **Hendrix, B.** (2019) Chronostratigraphy and terrestrial palaeoclimatology of Berriasian-Hauterivian strata of the Cedar Mountain Formation, Utah, USA. *Geological Society, London, Special Publications,* **498**,

Jones, H.L., and **Hajek, E.A.** (2007) Characterizing avulsion stratigraphy in ancient alluvial deposits. *Sedimentary Geology*, **202**, 124-137.

Kirkland, J.I., Cifelli, R.L., Britt, B.R., Burge, D.L., DeCourten , F.L., Eaton, J.G., and **Parrish, J.M.,** (1999) Distribution of vertebrate faunas in the Cedar Mountain Formation, east central Utah, in Gillette, D.D., ed., *Vertebrate Paleontology in Utah: Utah Geological Survey Miscellaneous Publication*, **1999–1**, 201–217.

Kowallis, B.J., Heaton, J.S., and **Bringhurst, K.** (1986) Fission-track dating of volcanically derived sedimentary rocks. *Geology*, **14**, 19-22.

Lazarus, E.D., and **Constantine, J.A.** (2013) Generic theory for channel sinuosity. *Proceedings of the National Academy of Sciences*, **110**, 8447-8452.

Leary, K.C.P., and **Ganti, V.** (2020) Preserved fluvial cross strata record bedform disequilibrium dynamics. *Geophysical Research Letters*, **47**, https://doi.org/10.1029/2019GL085910.

Ludvigson, G.A., Joeckel, R.M., Gonz¬lez, L.A., Gulbranson, E.L., Rasbury, E.T., Hunt, G.J., Kirkland, J.I., and **Madsen, S.** (2015) Correlation of Aptian-Albian carbon isotope excursions in continental strata of the Cretaceous foreland basin, Eastern Utah, U.S.A. *Journal of Sedimentary Research*, **80**, p. 955-974.

Ludvigson, G.A., Joeckel, R.M., Murphy, L.R., Stockli, D.F., Gonz¬lez, L.A., Suarez, C.A., Kirkland, J.I., and **Al-Suwaidi, A.** (2015) The emerging terrestrial record of Aptian-Albian global change. *Cretaceous Research*, **56**, 1-24.

Mahon, R.C., and **McElroy, B.** (2018) Indirect estimation of bedload flux from modern sand-bed rivers and ancient fluvial strata. *Geology*, **46**, 579-582.

Maizels, J.K. (1987) Plio-Pleistocene raised channel systems of the western Sharqiya (Wahiba), Oman. *Geological Society of London, Special Publications*, **35**, 31–50.

Maizels, J. (1990) Raised channel systems as indicators of palaeohydrologic change: a case study from Oman. *Palaeogeography, Palaeoclimatology, Palaeoecology*, **76**, 241–277.

Maizels, J., and **McBean, C.** (1990) Cenozoic alluvial fan systems of interior Oman: palaeoenvironmental reconstruction based on discrimination of palaeochannels using remotely sensed data. *Geological Society of London, Special Publications*, **49**, 565–582.

Mason, J., and **Mohrig, D.** (2018) Using time-lapse lidar to quantify river bend evolution on the meandering coastal Trinity River, Texas, USA. *Journal of Geophysical Research: Earth Surface*, **123**, 1133-1144.

Mason, J., and **Mohrig, D.** (2019a) Scroll bars are inner bank levees along meandering river bends. *Earth Surface Processes and Landforms,* **44**, 2649-2659.

Mason, J., and **Mohrig, D.** (2019b) Differential bank migration and the maintenance of channel width in meandering river bends. *Geology*, **47**, 1136-1140.

Mason, J. (2018) Sediment transport and the geomorphic evolution of the coastal Trinity River, TX. *PhD Dissertation, University of Texas at Austin,* 167 p.

McKee, E.D., and **Weir, G.W.** (1953) Terminology for stratification and cross-stratification in sedimentary rocks. *Geological Society of America Bulletin*, **64**, 381–390.

Meade, R.H. (1985) Wavelike movement of bedload sediment, East Fork River, Wyoming. *Environmental Geology and Water Sciences*, **7**, 215-225.

Miall, A.D. (1977) A review of the braided-river depositional environment. *Earth-Science Reviews*, **13**, 1-62.

Miall, A.D. (1985) Architectural-element analysis: a new method of facies analysis applied to fluvial deposits. SEPM *Special Publication-Recognition of Fluvial Depositional Systems and Their Resource Potential*, **19**, 33-81.

Miall, A.D. (1988) Architectural elements and bounding surfaces in fluvial deposits: anatomy of the Kayenta formation (lower Jurassic), Southwest Colorado. *Sedimentary Geology*, **55**, 233–262.

Miall, A.D. (2015) Updating uniformitarianism: stratigraphy as just a set of ‘frozen accidents’. *Geological Society of London, Special Publications,* **404**, 11-36.

Mohrig, D., Heller, P.L., Paola, C., and **Lyons, W.J.** (2000) Interpreting avulsion process from ancient alluvial sequences: Guadalope-Matarranya system (northern Spain) and

Wasatch Formation (western Colorado). *Geological Society of America Bulletin*, **112**, 1787–1803.

Mohrig, D., and **Smith, J.D.** (1996) Predicting the migration rates of subaqueous dunes. *Water Resources Research,* **32**, 3207-3217.

Nittrouer, J.A., Mohrig, D., Allison, M.A., and **Peyret, A.-P. B.** (2011a) The lowermost Mississippi River: a mixed bedrock-alluvial channel. *Sedimentology*, **58**, 1914-1934.

Nittrouer, J.A., Mohrig, D., and **Allison, M.** (2011b) Punctuated sand transport in the lowermost Mississippi River. *Journal of Geophysical Research: Earth Surface*, **116**, F04025.

Nuse, B. (2015) Flow processes and sedimentation in a low-sinuosity high net-sand content fluvial channel belt: 3D outcrop study of the Cedar Mountain Formation, Utah. *Unpublished MS Thesis, Colorado School of Mines.*

Owen, A., Nichols, G.J., Hartley, A.J., Weissmann, G.S., and **Scuderi, L.A.** (2015) Quantification of a distributive fluvial system: The Salt Wash DFS of the Morrison Formation, SW U.S.A. *Journal of Sedimentary Research*, **85**, 544-561.

Paola, C., and **Borgman, L.** (1991) Reconstructing random topography from preserved stratification. *Sedimentology,* **38**, 553-565.

Paola, C., Ganti, V., Mohrig, D., Runkel, A.C., and **Straub, K.M.** (2018) Time not our Time: Physical controls on the preservation and measurement of geologic time. *Annual Review of Earth and Planetary Sciences*, **46**, 409-438.

Parker, G., Paola, C., Whipple, K.X., and **Mohrig, D.** (1998) Alluvial fans formed by channelized fluvial and sheet flow. I: Theory: *Journal of Hydraulic Engineering*, **124**, 985-995.

Parker, G., Wilcock, P.R., Paola, C., Dietrich, W.E., and **Pitlick, J.** (2007) Physical basis for quasi-universal relations describing bankfull hydraulic geometry of single-thread gravel bed rivers. *Journal of Geophysical Research – Earth Surface*, **112**, F04005.

Peterson, F., and **Ryder, R.T.** (1975) Cretaceous rocks in the Henry Mountains region, Utah and their relation to neighboring regions. in *Four Corners Geological Society Guidebook,* **8**, p. 166-189.

Pizzuto, J.E. (1987) Sediment diffusion during overbank flows. *Sedimentology*, **34**, 301–317.

Reesink, A.J.H., and **Bridge, J.S.** (2011) Evidence of bedform superimposition and flow unsteadiness in unit-bar deposits, South Saskatchewan River, Canada. *Journal of Sedimentary Research*, **81**, 814-840.

Reesink, A.J.H., Van den Berg, J.H., Parsons, D.R., Amsler, M.L., Best, J.L., Hardy, R.J., Orfeo, O., and **Szupiany, R.N.** (2015) Extremes in dune preservation: Controls on the completeness of fluvial deposits. *Earth-Science Reviews*, **150**, 652-665.

Reesink, A.J.H. (2018) Interpretation of cross strata formed by unit bars. In eds. M.Ghinassi, L. Colombera, N.P. Mountney, and A.J.H. Reesink, *Fluvial Meanders and Their Sedimentary Products in the Rock Record, International Association of Sedimentary Petrologists Special Publication*, **48**, 173-200.

Reitz, M.D., Jerolmack, D.J., and **Swenson, J.B.** (2010) Flooding and flow path selection on alluvial fans and deltas. *Geophysical Research Letters*, **37**, L06401.

Rubin, D.M. (1987) Cross-bedding, Bedforms, and Paleocurrents. *SEPM Concepts in Sedimentology and Paleontology*, **1**.

Rubin, D.M., and **Hunter, R.E.** (1982) Bedform climbing in theory and nature. *Sedimentology*, **29**, 121–138.

Rubin, D.M., and **Hunter, R.E.** (1987) Bedform alignment in directionally varying flows. *Science*, **237**, 276-278.

Sable, V.H. (1956) Photogeologic map of the Tidwell-2 quadrangle, Emery and Grand counties, Utah. *Miscellaneous Geologic Investigation*, **Map I-162**.

Sadler, P.M. (1981) Sediment accumulation rates and the completeness of stratigraphic sections. *The Journal of Geology*, v. 89, 569-584.

Sadler, P.M., and **Jerolmack, D.J.** (2015) Scaling laws for aggradation, denudation and progradation rates: the case for time-scale invariance at sediment sources and sinks. *Geological Society of London, Special Publications,* **404**, 69-88.

Seminara, G., and **Tubino, M.** (1989) Alternate bars and meandering: Free, forced and mixed interactions. In S. Ikeda and G. Parker (Eds.), River Meandering: Water Resources Monograph, **12**, 267-320. American Geophysical Union: Washington, D.C.

Shaw, J.B., and **Mohrig, D.** (2014) The importance of erosion in distributary channel network growth, Wax Lake Delta, Louisiana, USA: *Geology*, **42**, 31-34.

Skelly, R.L., Bristow, C.S., and **Ethridge, F.G.** (2003) Architecture of channel-belt deposits in an aggrading shallow sandbed braided river: the lower Niobrara River, northeast Nebraska. *Sedimentary Geology*, **158**, 249-270.

Slingerland, R., and **Smith, N.D.** (2004) River avulsions and their deposits. *Annual Review of Earth and Planetary Sciences,* **32**, 257-285.

Stokes, W.L. (1961) Fluvial and Eolian Sandstone Bodies in Colorado Plateau. *AAPG SP-Geometry of Sandstone Bodies*, **22**, 151–178.

Stouthamer, E., and **Berendsen, H.J.A.** (2001) Avulsion frequency, avulsion duration, and interavulsion period of Holocene channel belts in the Rhine-Meuse Delta, the Netherlands. *Journal of Sedimentary Research*, **71**, 589-598.

Swanson, T., Mohrig, D., Kocurek, G., Perillo, M., and **Venditti, J.** (2018) Bedform spurs: a result of a trailing helical vortex wake. *Sedimentology*, **65**, 191-208.

Swanson, T., Mohrig, D., Kocurek, G., Cardenas, B.T., and **Wolinsky, M.A.** (2019) Preservation of autogenic processes and allogenic forcings within set-scale aeolian architecture I: numerical experiments. *Journal of Sedimentary Research,* **89,** 728-740.

Swartz, J.M., Mohrig, D., Passalacqua, P., Goff, J., and **Gulick, S.P.S.** (2018) From distributary to tributary: coastal drainage network position and morphometry are set by depositional processes. *Presented at the American Geophysical Union 2018 Fall Meeting*, EP21B-2230.

Van De Lagewag, W.Y., Van Dijk, W.M., and **Kleinhans, M.G.** (2013) Channel belt architecture formed by a meandering river. *Sedimentology*, **60**, 840-859.

Wang, J., and **Bhattacharya, J.P.** (2017) Plan-view paleochannel reconstruction of amalgamated meander belts, Cretaceous Ferron Sandstone, Notom Delta, south-central Utah, U.S.A. *Journal of Sedimentary Research*, **88**, 58–74.

Whiting, P.J., and **Dietrich, W.E.** (1993) Experimental constraints on bar migration through bends: Implications for meander wavelength selection. *Water Resources Research*, **29**, 1091-1102.

Williams, R.M.E., Irwin, R.P., and **Zimbelman, J.R.** (2009) Evaluation of paleohydrologic models for terrestrial inverted channels: Implications for application to Martian sinuous ridges. *Geomorphology*, **107**, 300–315.

Williams, R.M.E., Chidsey Jr., T.C., and Eby, D.E. (2007) Exhumed Paleochannels in Central Utah—Analogs for Raised Curvilinear Features on Mars. *Central Utah-Diverse Geology of a Dynamic Landscape*, 221–235.

Wright, S., and **Parker, G.** (2003) Grain-size specific suspended sediment transport and flow resistance in large sand-bed rivers. In A. Gyr and W. Kinzelbach (Eds.), Sedimentation and Sediment transport, 221-227. Netherlands: Springer.

Wu, C., Bhattacharya, J.P., and **Ullah, M.S.,** (2015) Paleohydrology and 3D facies architecture of ancient point bars, Ferron Sandstone, Notom Delta, South-central Utah, USA. *Journal of Sedimentary Research*, **85**, 399–418.

Wu, C., Ullah, M.S., Lu, J., and **Bhattacharya, J.P.** (2016) Formation of point bars through rising and falling flood stages: Evidence from bar morphology, sediment transport and bed shear stress. *Sedimentology*, **63**, 1458–1473.

Young, R.G. (1960) Dakota Group of Colorado Plateau. *American Association of Petroleum Geologists Bulletin*, **44**, 158-194.

Zaki, A.S., Pain, C.F., Edgett, K.S., and **Giegengack, R.** (2018) Inverted stream channels in the Western Desert of Egypt. Synergistic remote, field observations and laboratory analysis on Earth with applications to Mars. *Icarus*, **309**, 105-124.

FIGURES

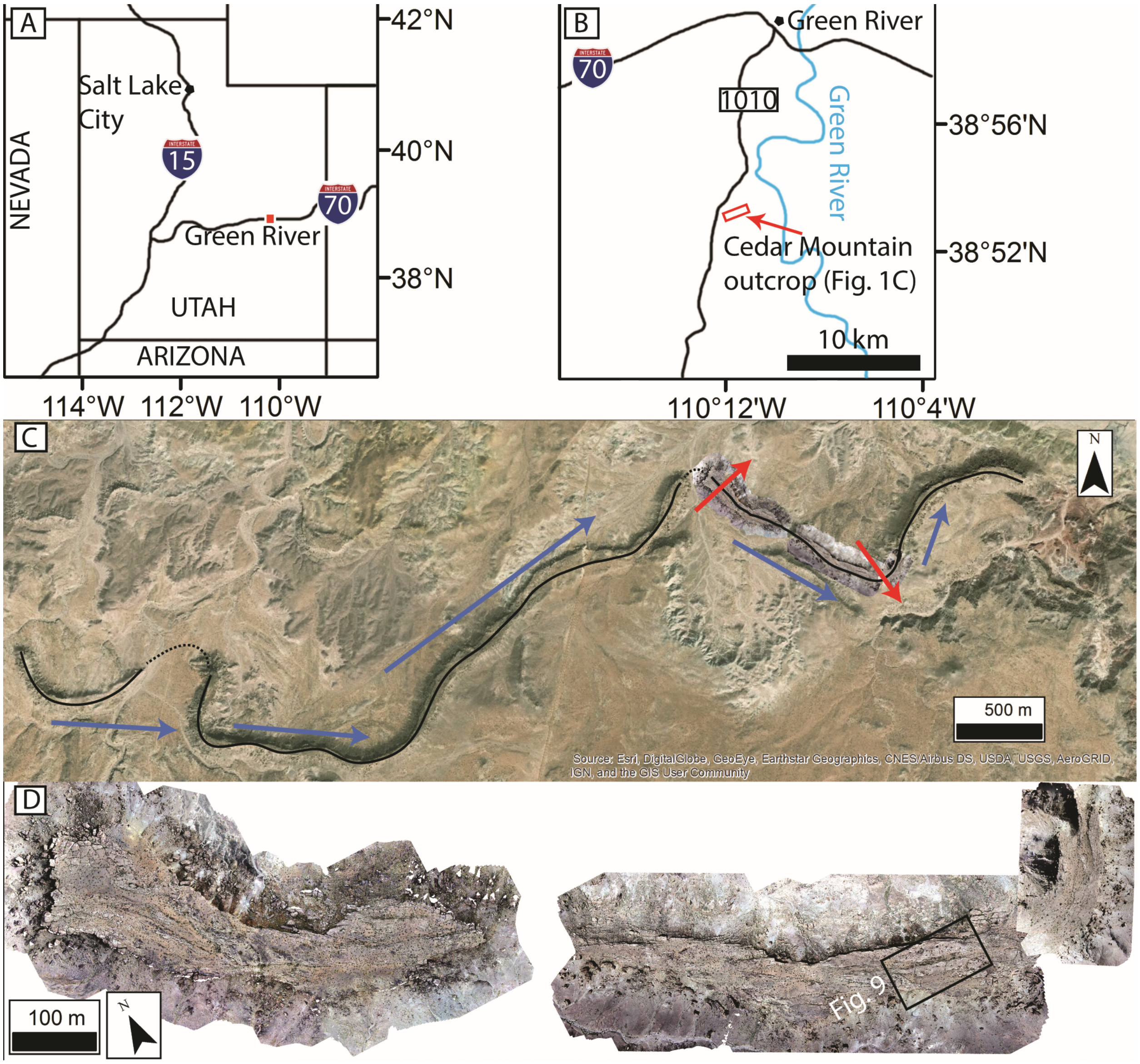

Figure 1 – (A) Index map of Utah. (B) Enlargement near Green River, showing the location of the town as well as the studied ridges of the Cedar Mountain Formation and the Morrison Formation south of town along 1010. (C) View showing the ridges beyond the study area. Black line maps out a ridge centerline for several km, with interpreted dashed segments bridging erosional discontinuities. Teal arrows show the general direction of paleoflow. Red arrows mark

the two major bends bounding the studied part of the ridge. The arrows point away from the center of curvature, and match with the general dip directions of local dipping bar strata. (D) Drone ortho-images of the studied eastern and western ridges of the Cedar Mountain Formation ridges. The photomosaics are rotated slightly to fit the panel, but are correctly co-located.

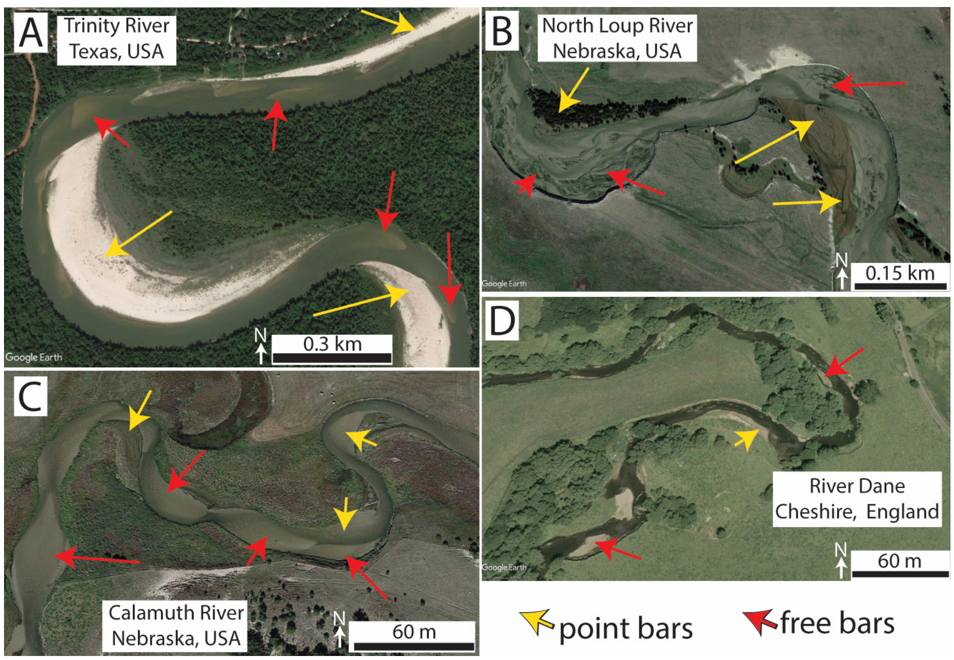

Figure 2 – Free bars (red arrows) and point bars (yellow arrows) commonly coexist in rivers, both in straight reaches and bends. (A) Trinity River, Texas, USA. Image centered at 30.134° N, -94.815° E. (B) North Loup River, Nebraska, USA. Image centered at 42.019° N, -100.098° E. (C) Calamuth River, Nebraska, USA. Image centered at 42.083° N, -99.649° E. (D) River Dane, Cheshire, England. Image centered at 53.183° N, -2.259° E.

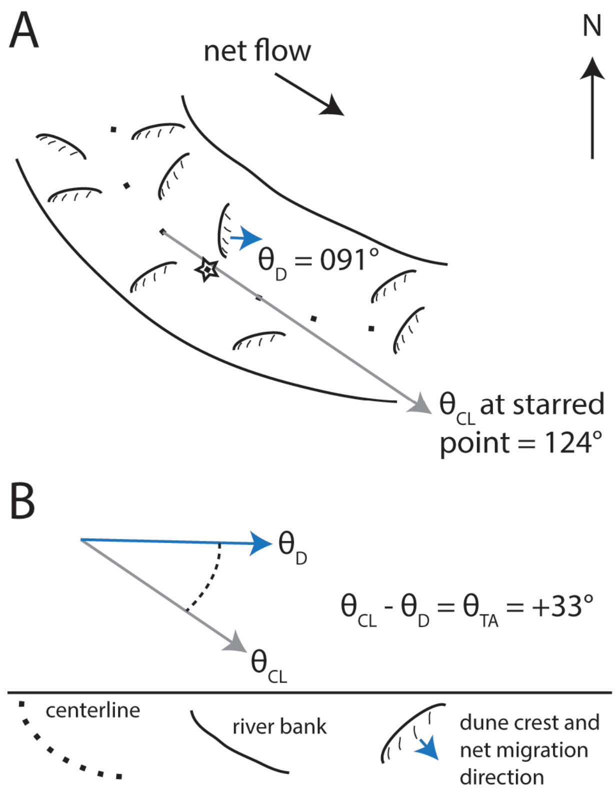

Figure 3 – (A) Diagram defining the components of the transport anomaly, Θ_{TA}, for a modern river channel. A measurement of transport direction, Θ_D, is made from the orientation of a dune crest (short black arrow; 091°). The centerline point closest to the measurement of Θ_D is starred. The orientation of the starred centerline point, Θ_{CL}, is defined as the azimuth direction of the ray originating at the adjacent upstream point and passing through the adjacent downstream point (gray arrow; 124°). (B) The transport anomaly, Θ_{TA}, is defined as $\Theta_{CL} - \Theta_D$. It may be positive or negative, and is bound between -180° and positive 180°. In this scenario, Θ_{TA} = 124° - 091° = 33°.

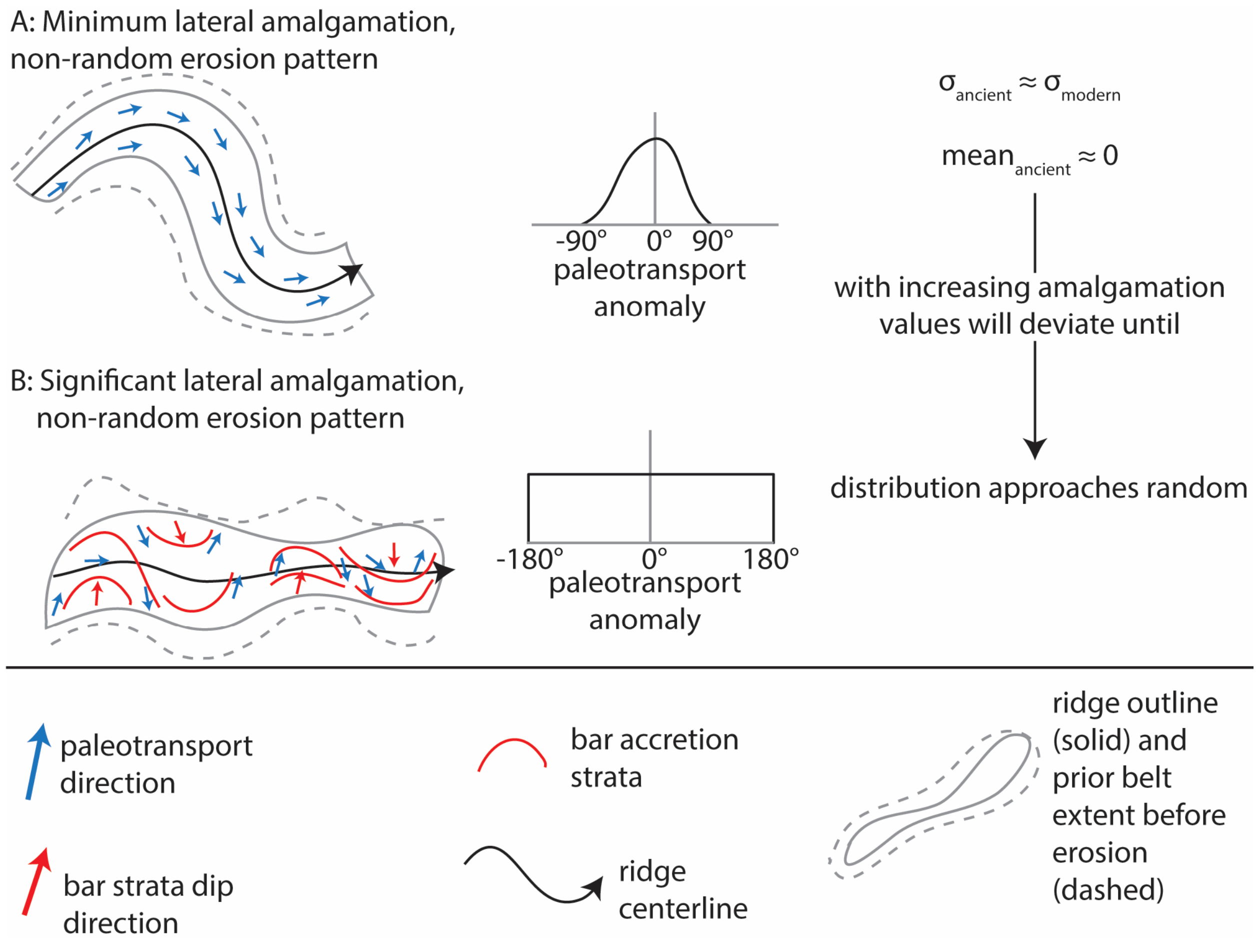

Figure 4 – Hypothesized scenarios guiding interpretations of paleotransport anomaly results. Schematic diagrams are on the left, the distribution of paleotransport anomaly measurements are in the middle, and relevant statistical moments are on the right. Standard deviation is shown by σ. Legend is at the bottom. (A) The ridge centerline represents well the formative channel centerline. With increasing lateral amalgamation, results will instead approach the scenario in panel B. (B) Lateral amalgamation of the channel-belt separates any formative channel centerline from the ridge centerline. Laterally accreting bar strata are preserved. A random exhumation pattern not following the edges of the channel belt is unlikely to show any of these patterns.

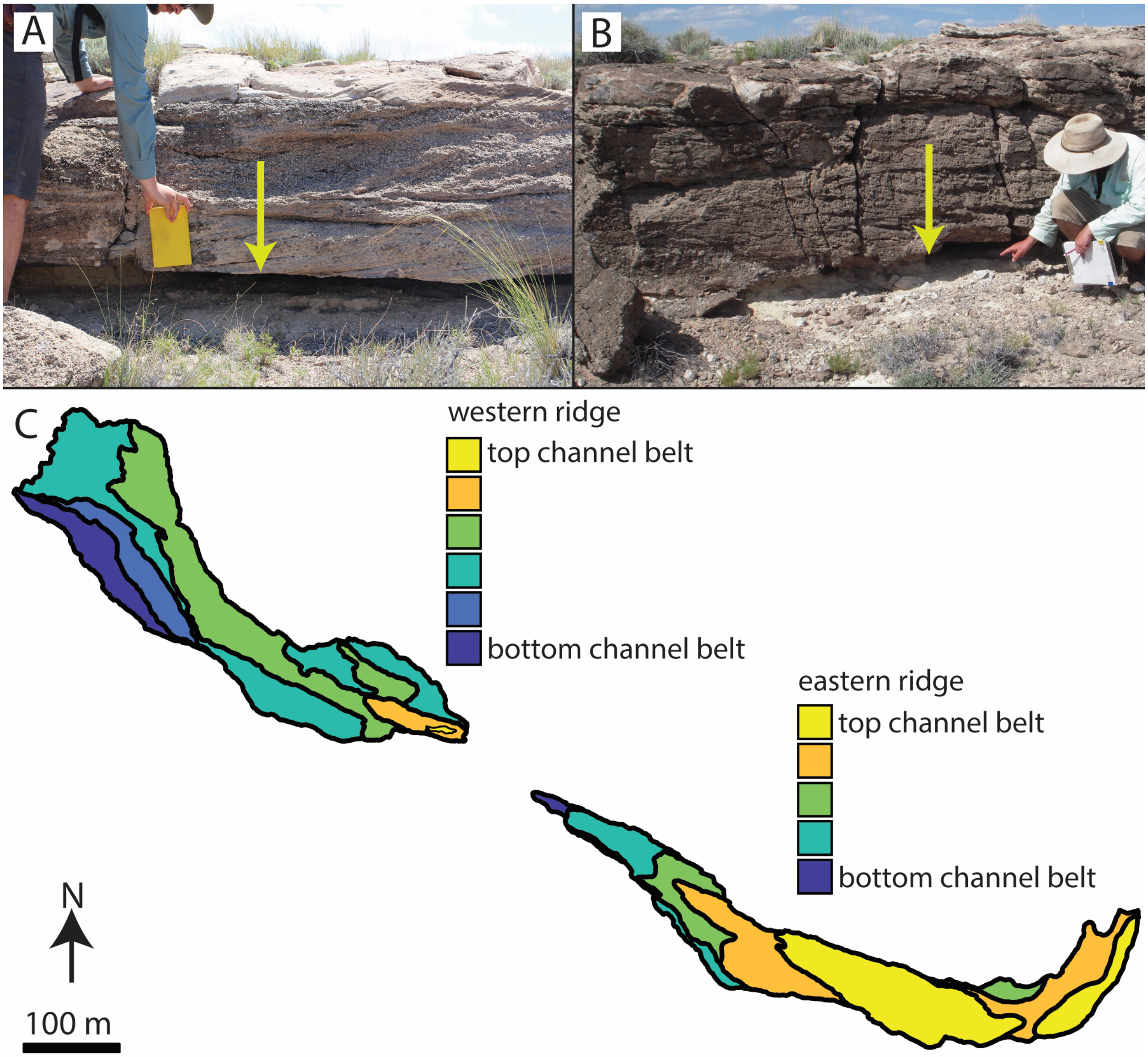

Figure 5 – (A-B) Yellow arrows pointing to erosional surfaces above friable, recessed mudstones separating coarse-grained, cross-bedded packages. These erosional surfaces are interpreted to represent the contacts between stacked channel belts. (C) Geologic maps showing the stacking patterns of channel-belts exposed at the surface of both ridges. There is no attempt to correlate individual channel belts between ridges.

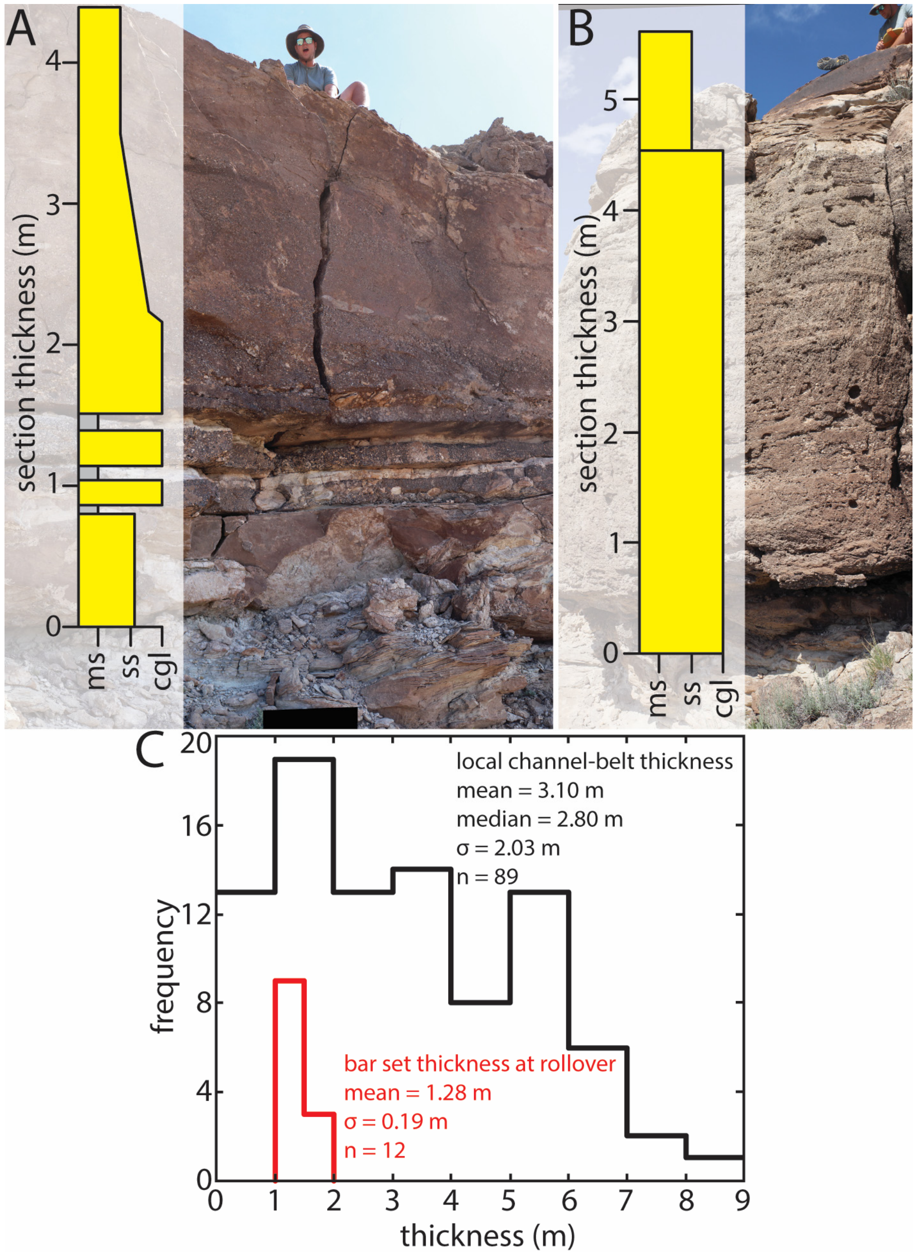

Figure 6 – (A) Vertical section showing story-bounding surfaces and associated mudstones. Stories in this section are of average to below-average thickness. (B) Two stories bounded by an erosional surface with no associated mudstone. The bottom story is above average thickness. (C) Histogram of local channel-belt (story) thicknesses measured from vertical sections, and the mean thickness of a bar set at the rollover (red line), which is used as a proxy for channel depth.

The difference between channel depth and channel-belt thickness is due to aggradation of the channel bed.

Figure 7 - Photo of dune cross strata exposed in planview along upper ridge surfaces. Blue arrow shows the mean dip directions of cross strata. This 3-D outcrop shows the relationship between planform-exposed cross strata and vertically exposed cross strata. Boots for scale.

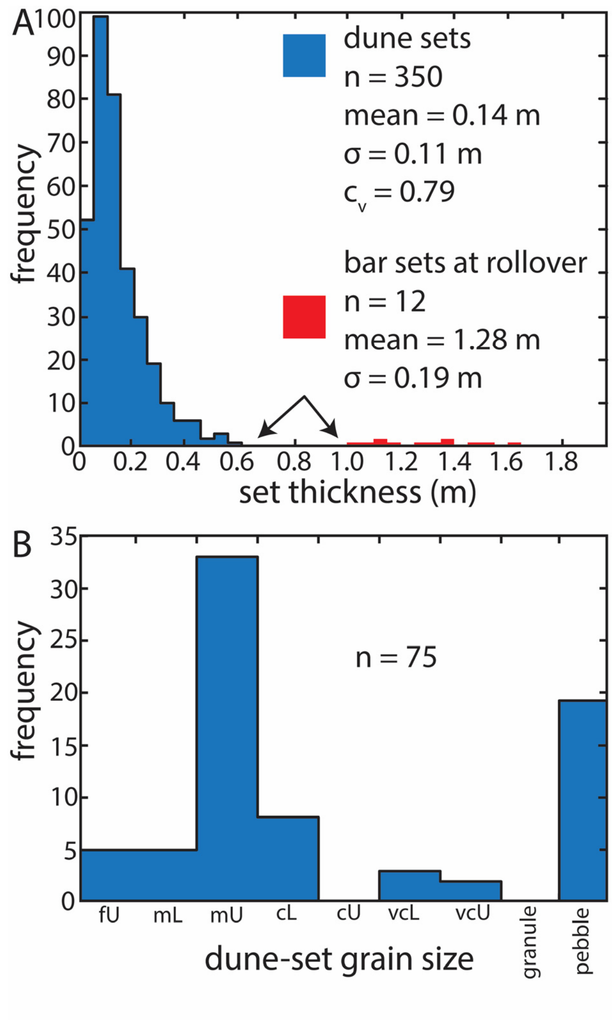

Figure 8 – (A) Histograms showing the distribution of dune and bar cross-set thicknesses, with statistical moments and the coefficient of variation (c_v). Arrows highlight a break between the two distributions when measuring bar sets at a rollover. (B) Distribution of grain-size classes in dune cross sets. Classes labeled fU, mL, mU, cL, cU, vcL, and vcU represent sand sizes of fine upper, medium lower, medium upper, coarse lower, coarse upper, very coarse lower, and very coarse upper, respectively.

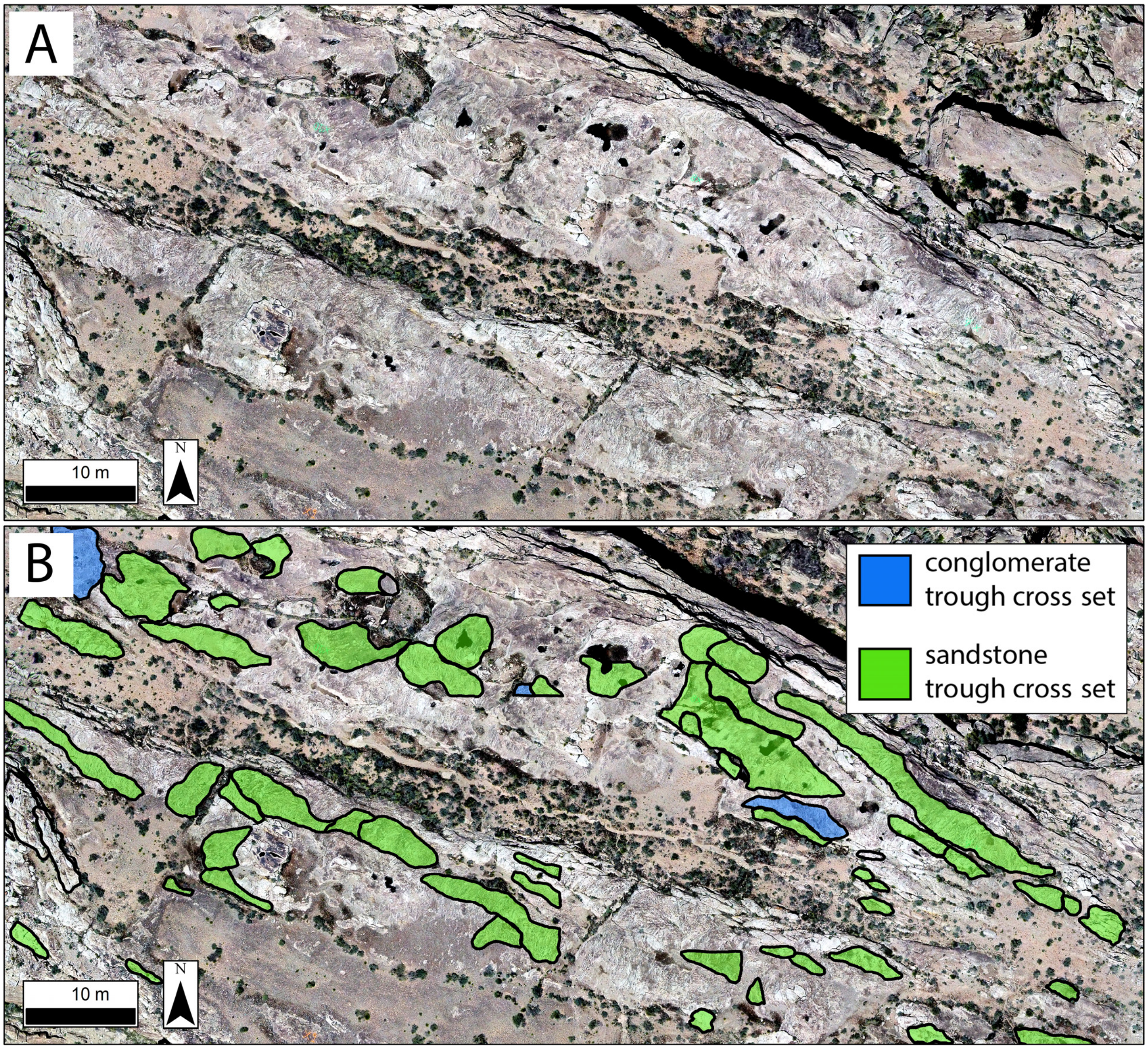

Figure 9 – (A) Example of drone photomosaics used as field base maps. (B) Digitized field map showing planform-exposed sets of cross strata outlined and filled in with green (sandstone) or blue (pebble conglomerate).

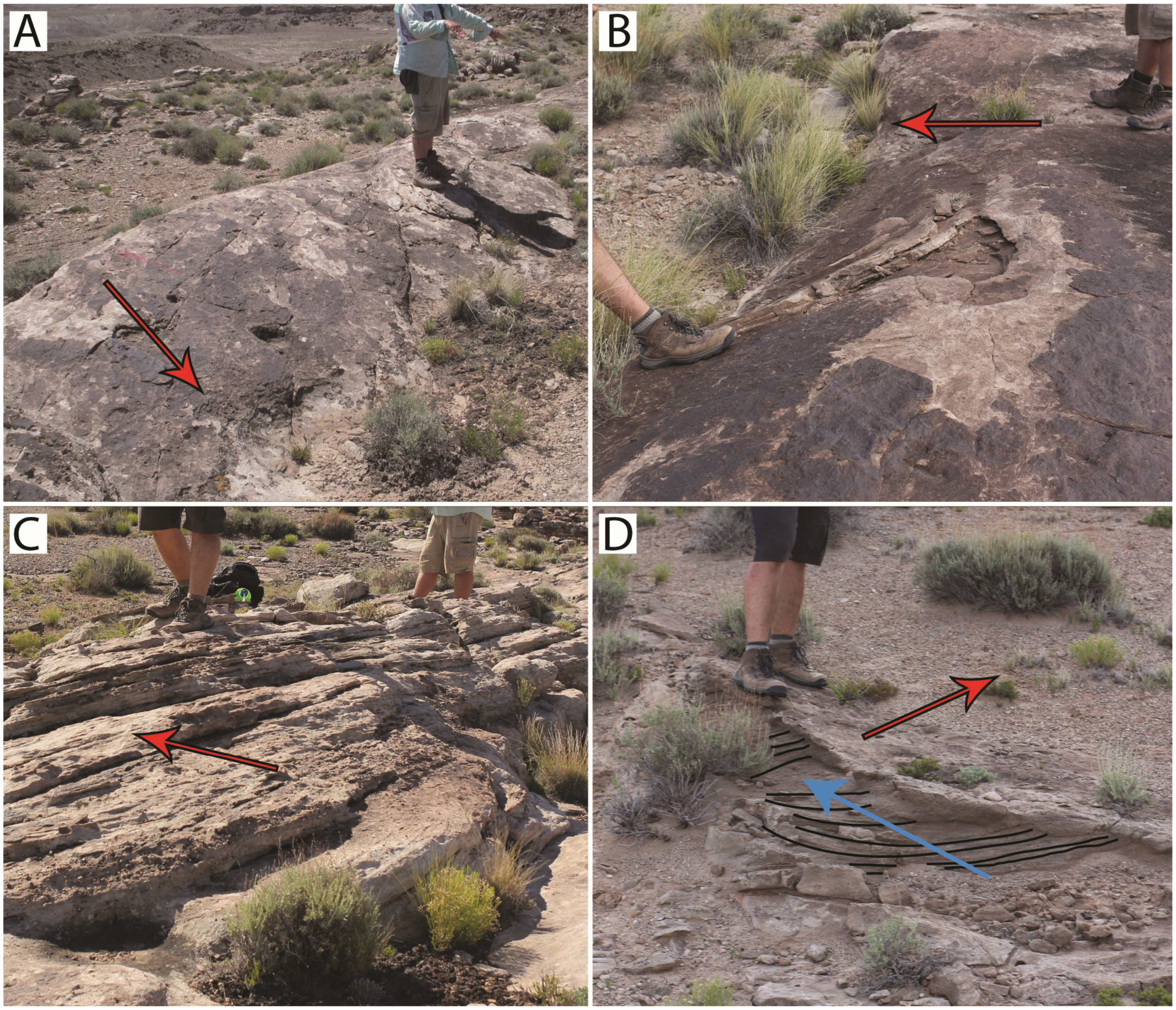

Figure 10 - Examples of larger-scale accretion strata. Red arrows show the dip direction of the strata in each panel. (A) A lack of exposed bounding surfaces on this topographic surface suggests the topography itself represents a bounding surface. (B) Beneath the arrow, erosion exposes internal stratification parallel to the surface. (C) A 3-D outcrop of larger-scale dipping strata composed of smaller-scale stratification exposed by erosion. (D) Compound cross strata with a larger-scale accretion surface (red arrow) dipping obliquely to a smaller-scale dune set (blue arrow). A few dune cross strata are mapped in black lines.

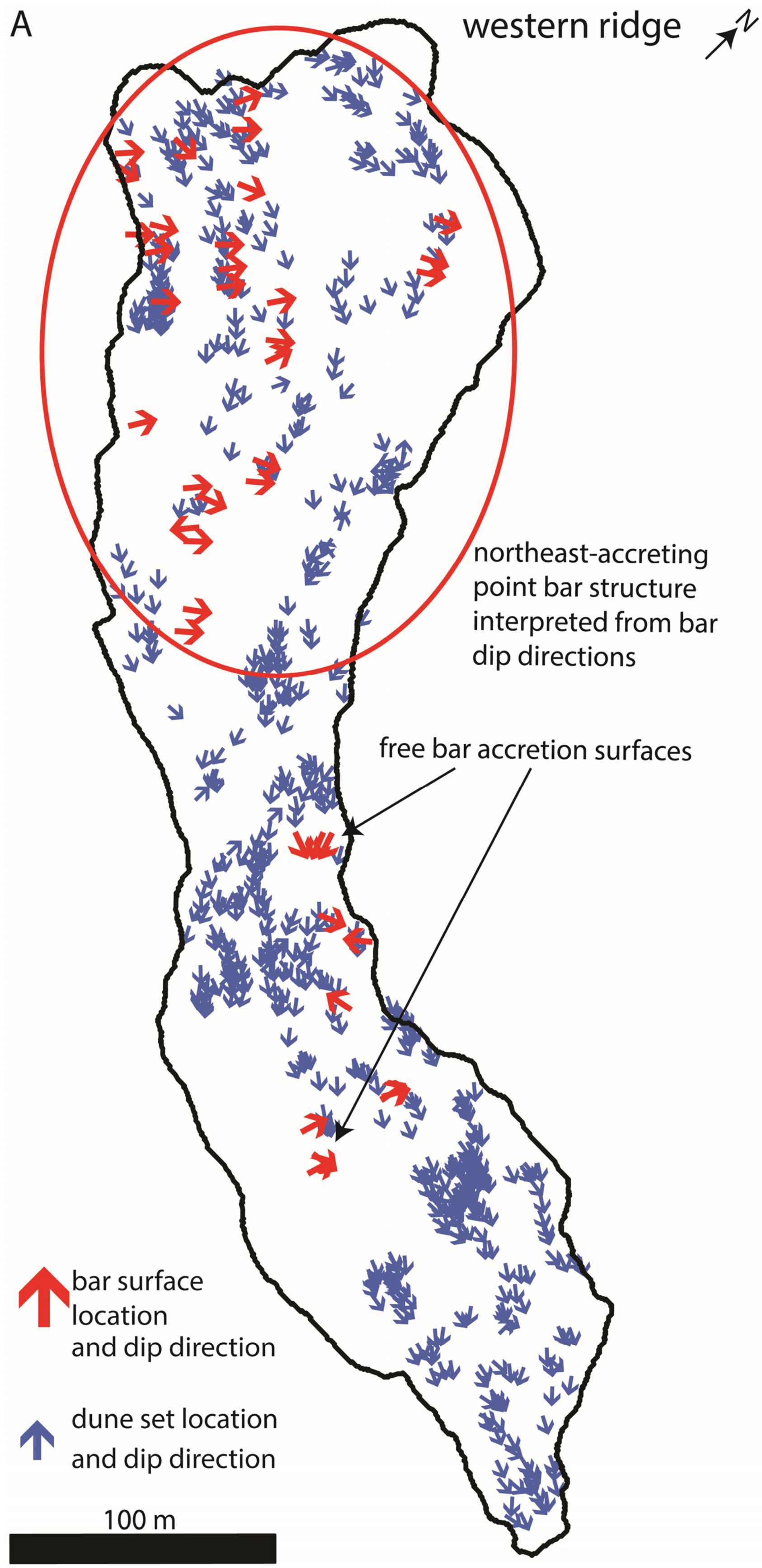
A
western ridge
N
northeast-accreting
point bar structure
interpreted from bar
dip directions
free bar accretion surfaces
bar surface
location
and dip direction
dune set location
and dip direction
100 m

981

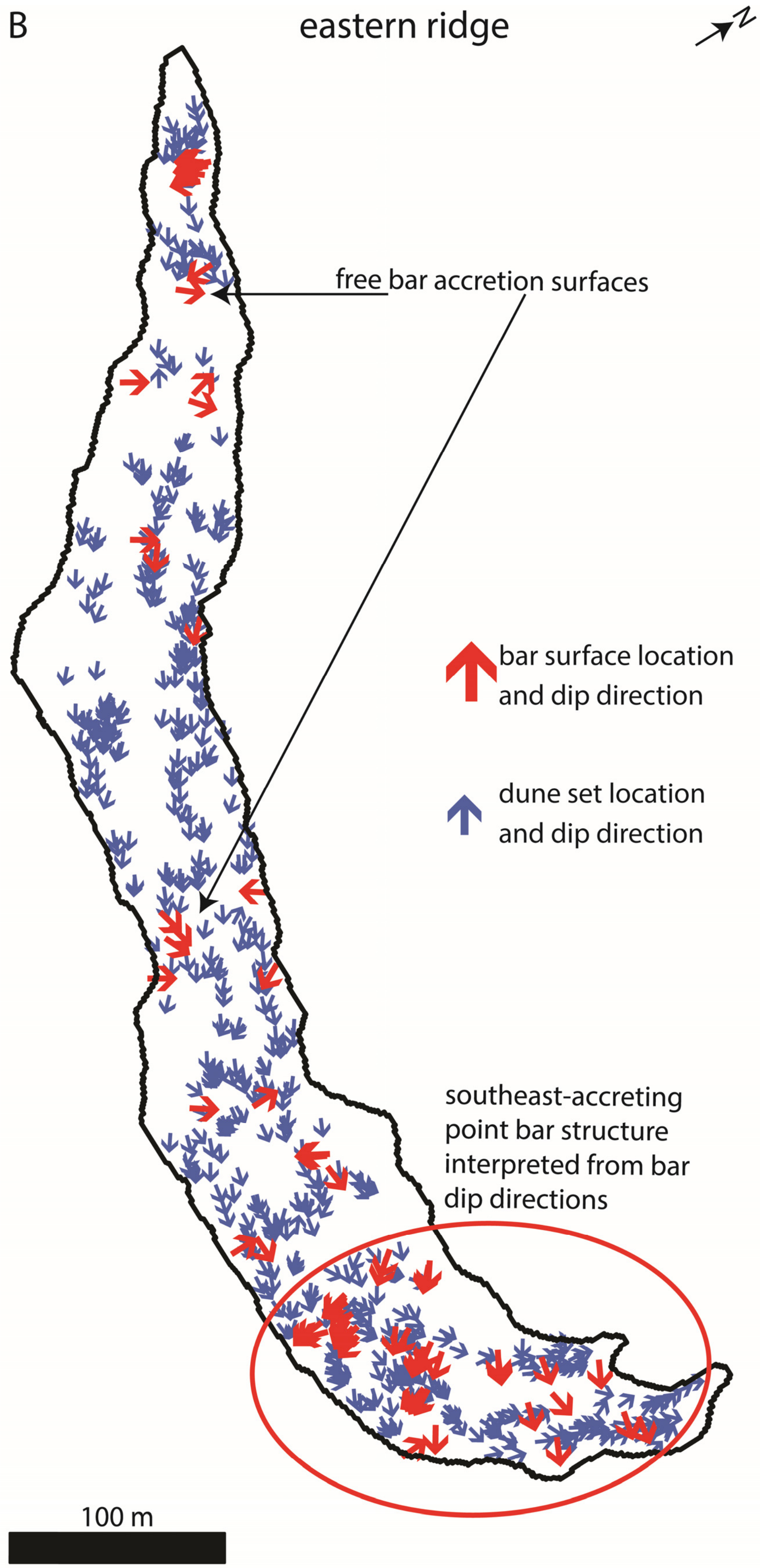
B
eastern ridge
N
free bar accretion surfaces
bar surface location
and dip direction
dune set location
and dip direction
southeast-accreting
point bar structure
interpreted from bar
dip directions
100 m

982

Figure 11 – Planform maps outlining the top surfaces of the western (A) and eastern (B) ridges. Two locations with clusters of similarly dipping bar accretion surfaces following ridge curvature are interpreted to represent point bars. The northeast-accreting point bar structure of the western ridge corresponds with a larger-scale ridge curvature beyond the extent of the study area (Fig. 1C). Bar accretion surfaces not clearly associated with a point bar are interpreted as free-bar accretion surfaces.

Figure 12 – The preservation of bar topography on upper-ridge surfaces. (A) Fisheye view of a sandstone mound rising towards the downstream direction (left to right), with a surface

defined by shingled cross-sets climbing with topography. This is interpreted as the stoss surface of a downstream-migrating barform. Tape measure for scale in foreground, arrow pointing to person in background. (B) Interpretation of panel A. (C) Downstream end of sandstone mound featuring cross sets and topography falling in the downstream direction. Interpreted as the lee slope of a downstream-migrating barform. Person for scale (1.65 m tall). (D) Interpretation of panel C.

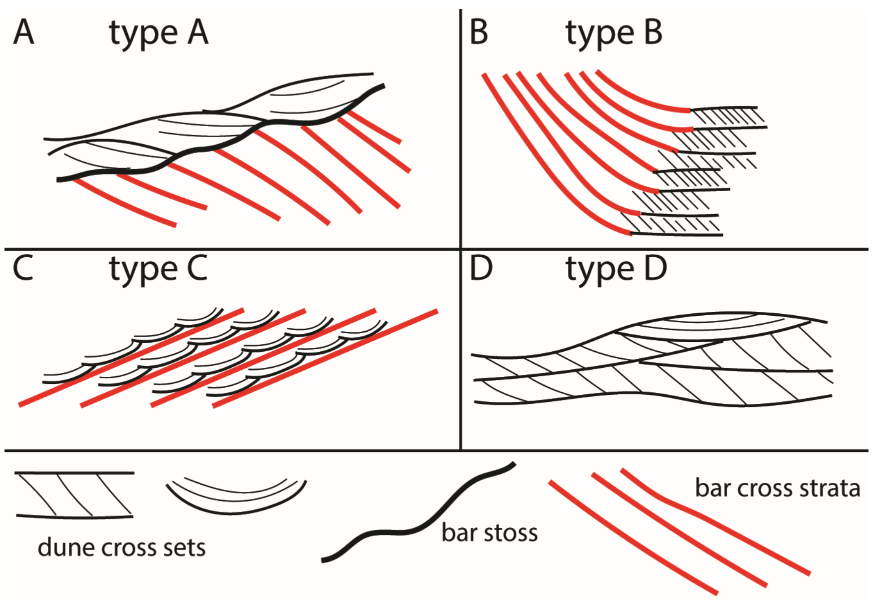

Figure 13 – The four arrangements of compound dune and bar strata. A: Type A strata have a bar set beneath dune cross-sets, separated by an upstream-dipping surface. B: Type B strata have bar sets shallowing and thickening downstream, where they conformably become dune cross sets. C: Type C strata show compound dune and bar strata dipping at high angles to each other. D: Type D strata are dune sets with no clear compound structure.

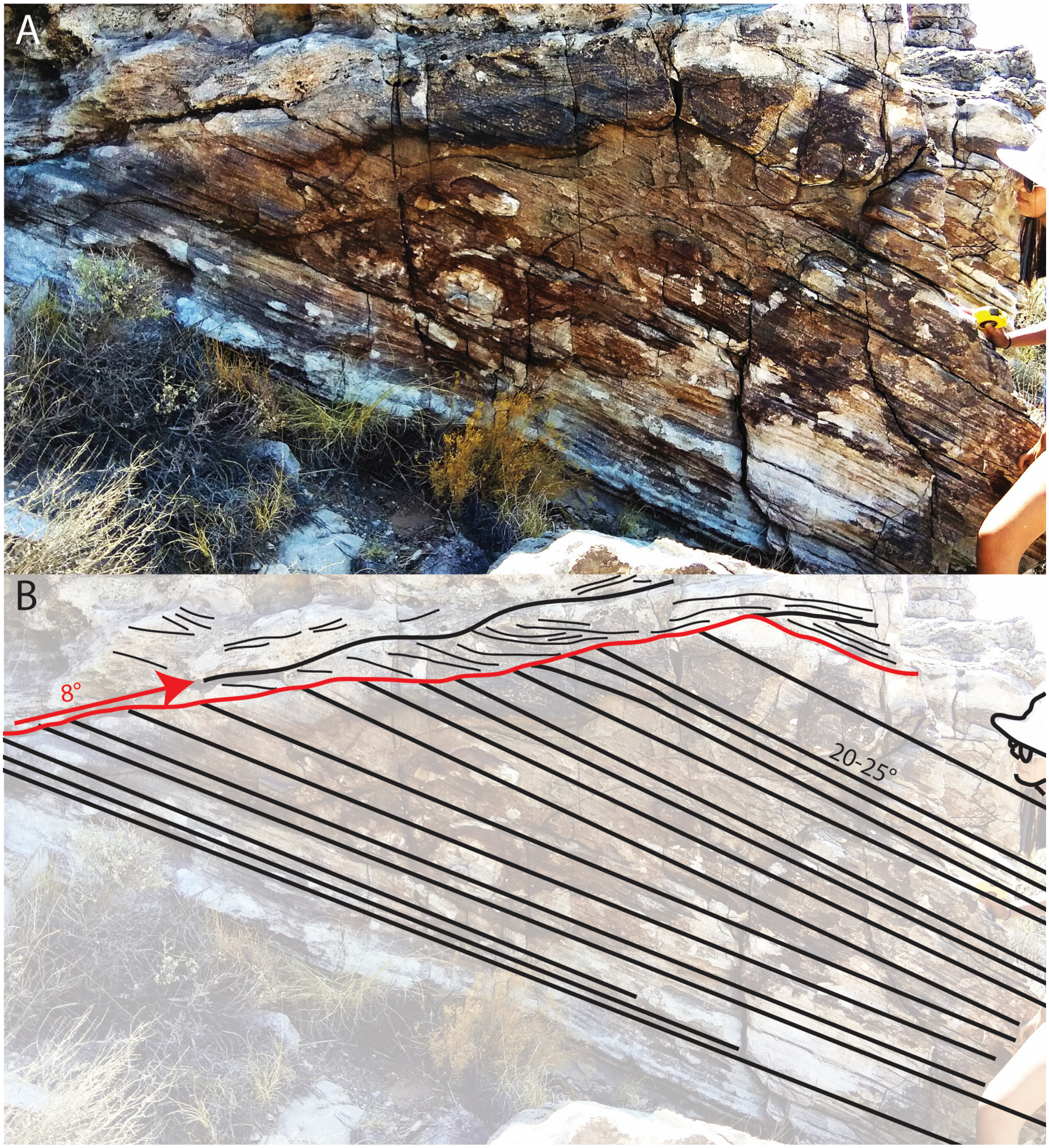

1004

1005

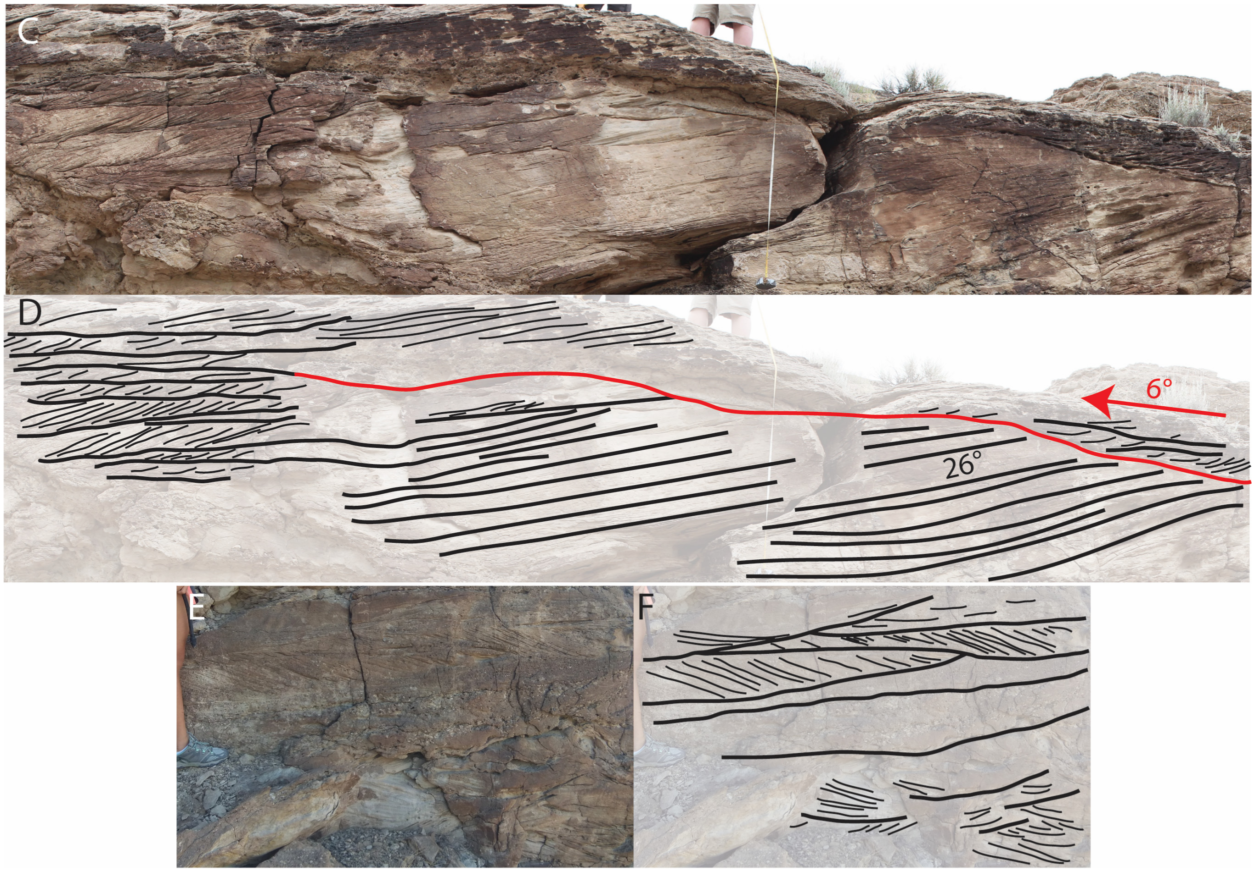

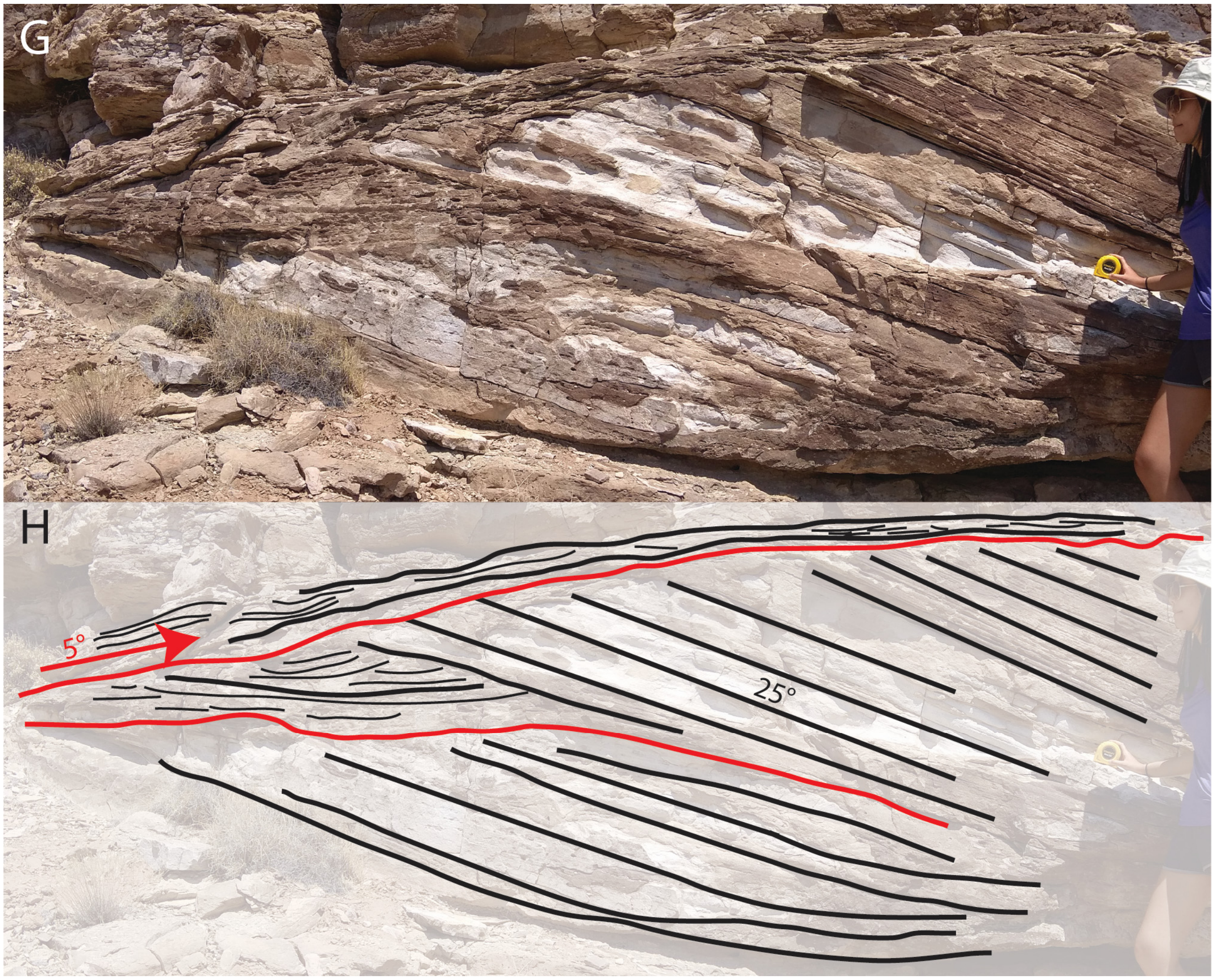

Figure 14 - Cross-sectional view of Type A-D strata (Fig. 13), with superimposed interpretations. Sets of dune and bar strata are marked by thick black lines and dune cross strata by thinner black lines. Surfaces separating dune and bar strata are marked by red lines. (A-B) Type A strata from the stoss side of a bar, with an interpreted transition to the lee side. Flow was from left to right. (C-D) Cross-sectional view of preserved strata from the lee (Type B) and stoss (Type A) sides of a bar form. Flow was from right to left. (E-F) Cross-sectional view of Type D strata featuring a ±90° spread in transport direction, conglomerates, and a lack of bar architecture. This type of architecture is interpreted as a thalweg environment due to the coarser grains

driven by higher velocity flow, and a larger spread in transport driven by changes in steering due to bar growth. (G-H) Cross-sectional view showing the internal structure of a barform with Type A strata overlying Type B strata. Flow was from left to right. From bottom to top, the transition from stoss-to-lee architecture to lee architecture, all within the same barform, records the forward migration and aggradation of the barform.

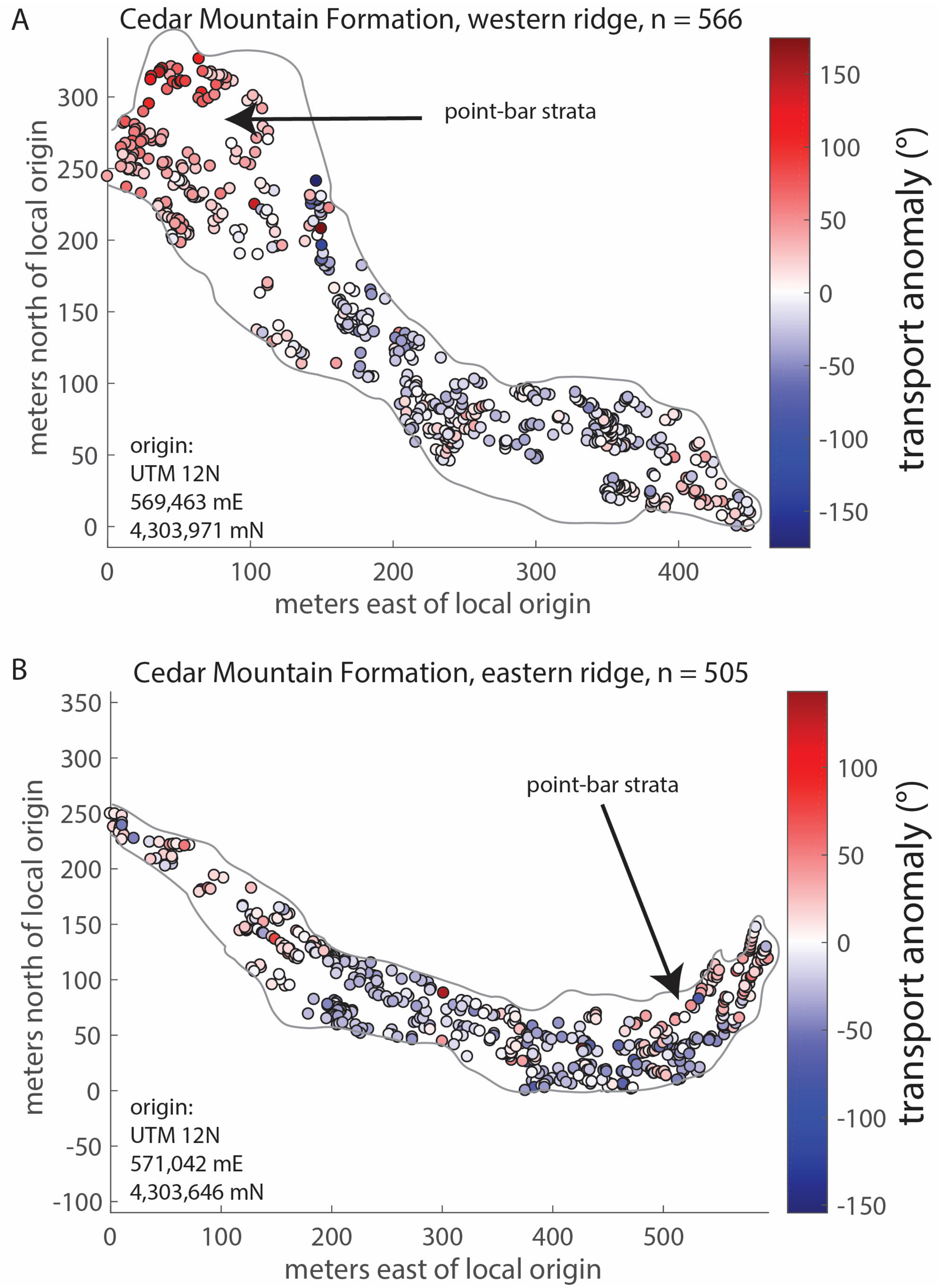

A
Cedar Mountain Formation, western ridge, n = 566
point-bar strata
meters north of local origin
meters east of local origin
origin:
UTM 12N
569,463 mE
4,303,971 mN
transport anomaly (°)
B
Cedar Mountain Formation, eastern ridge, n = 505
point-bar strata
meters north of local origin
meters east of local origin
origin:
UTM 12N
571,042 mE
4,303,646 mN
transport anomaly (°)

1020

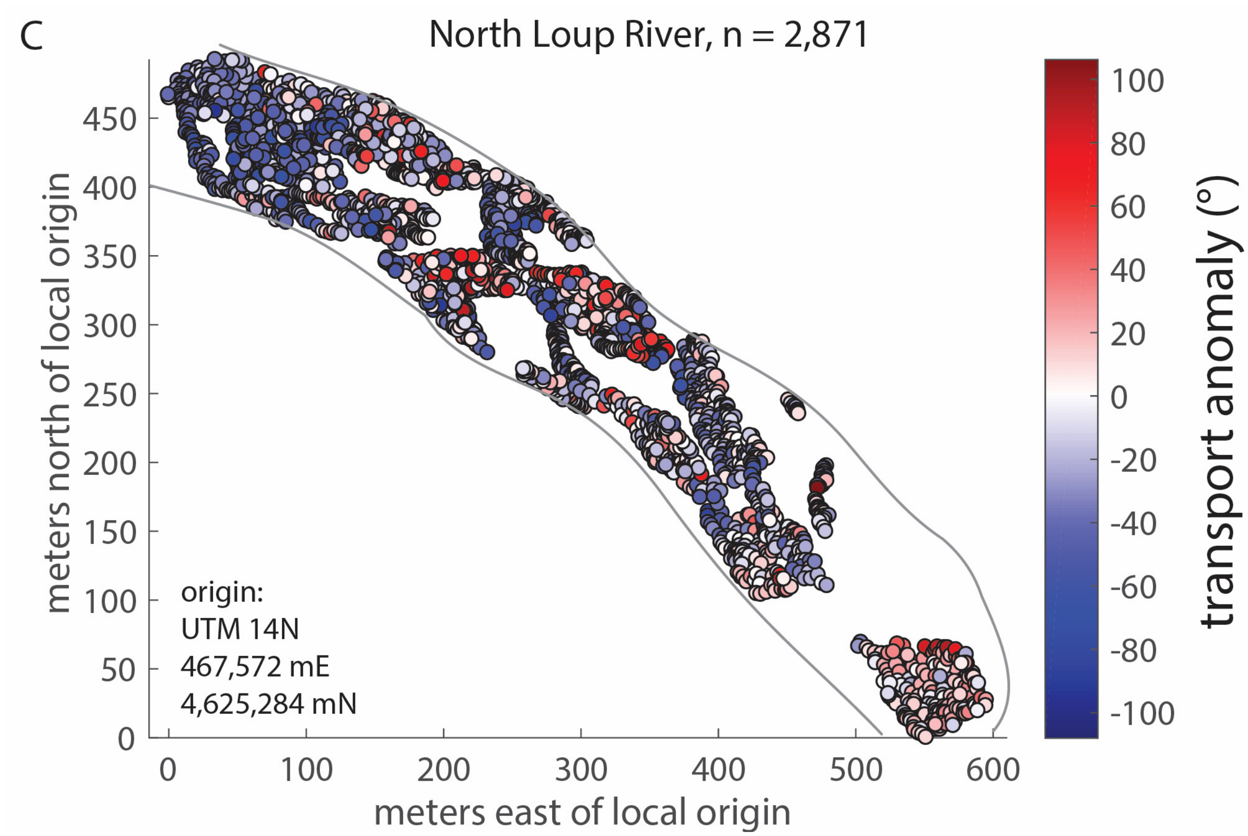

Figure 15 – Transport anomaly maps of the western ridge of the Cedar Mountain Formation (A), the eastern ridge (B), and the North Loup River (C). X and Y coordinates are relative to a different local datum in each map, shown in the bottom left corner of each panel. Circles show the location of paleotransport or modern transport direction measurements. The color at each point represents the paleotransport or transport anomaly (Fig. 3A-B). Colors are stretched to each individual panel. Gray lines represent ridge outlines and the banks of the North Loup River. Black arrows in panels A and B point to regions recording point bar accretion, and are associated with relatively high anomaly values, particularly in the western ridge (Figs. 1C and 11).

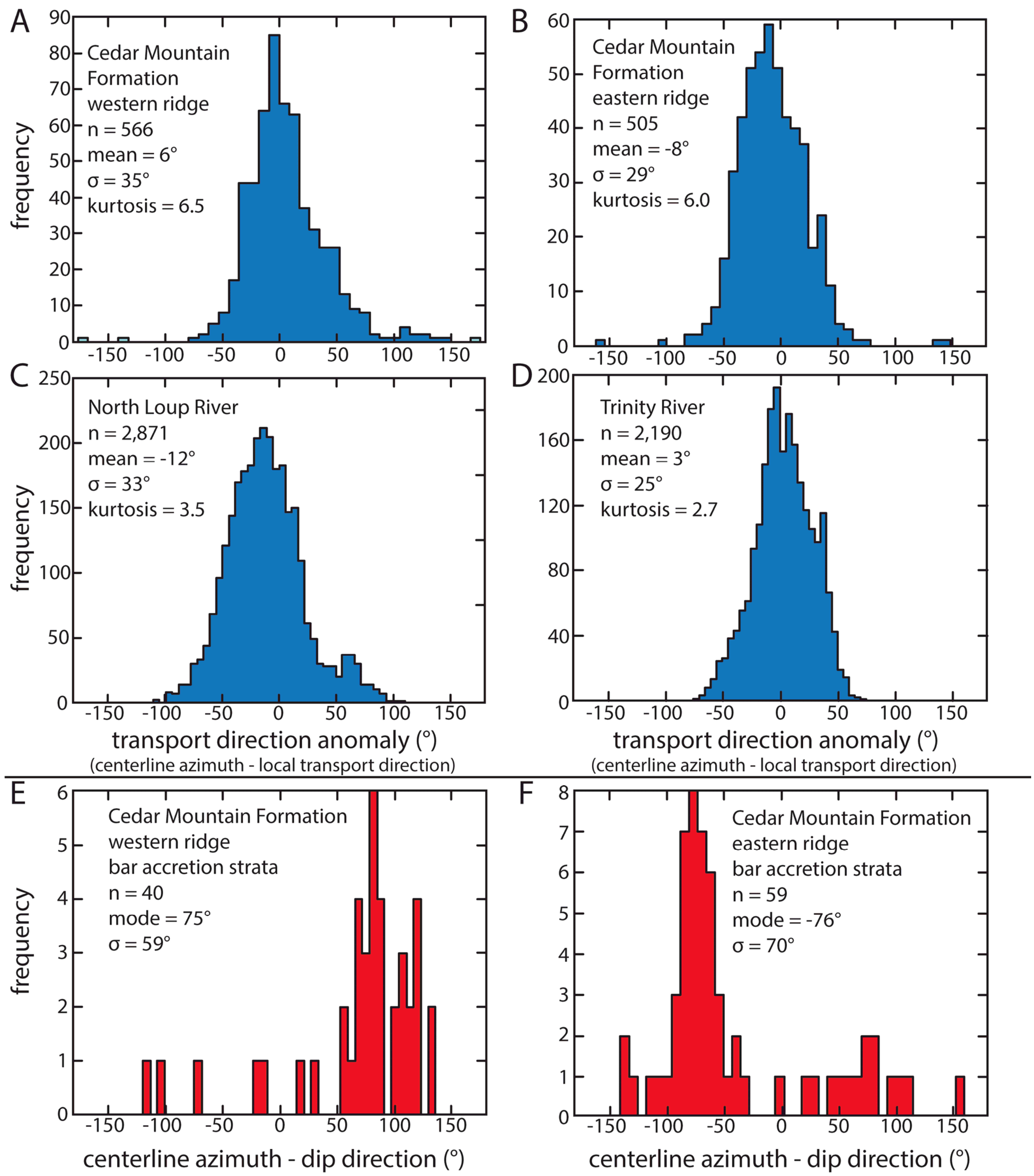

1031

1032 Figure 16 – Histograms showing the distribution of paleotransport/transport anomalies of the
1033 western (A) and eastern (B) ridges of the Cedar Mountain Formation, and the modern North
1034 Loup River (C) and Trinity River (D). The number of measurements, mean, and standard

deviation are reported in each panel. Note the similarity in mean and standard deviation between the ancient and modern datasets. Histograms (E) and (F) show the difference between dip directions of bar accretion strata exposed along the upper surfaces of ridges and the centerline. Both histograms show a wide distribution of values with peaks approaching perpendicular to the centerline trend.

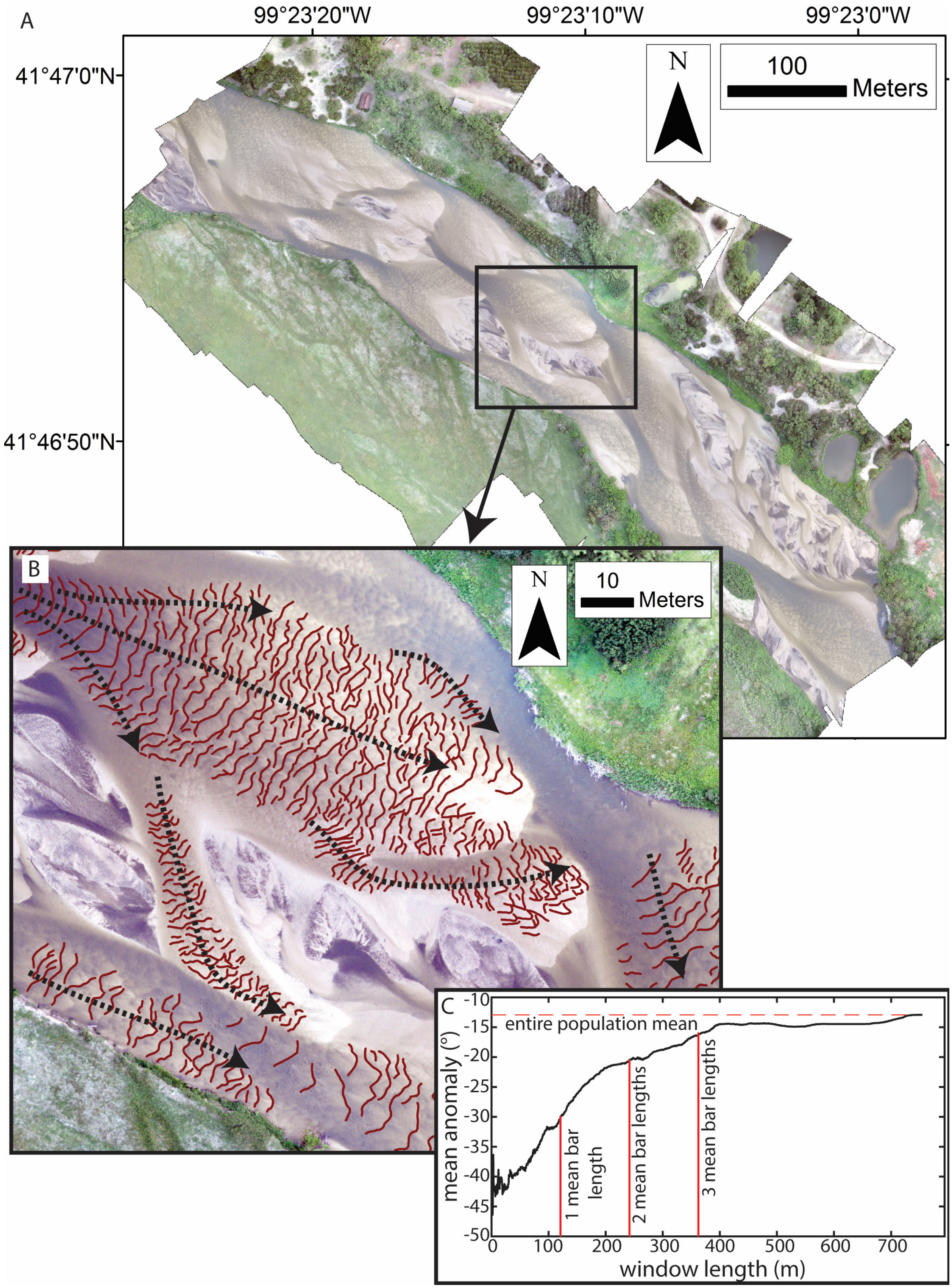
A
99°23'20"W
99°23'10"W
99°23'0"W
41°47'0"N
41°46'50"N
N
100
Meters
B
N
10
Meters
C
mean anomaly (°)
-10
-15
-20
-25
-30
-35
-40
-45
-50
entire population mean
1 mean bar length
2 mean bar lengths
3 mean bar lengths
0
100
200
300
400
500
600
700
window length (m)

Figure 17 – (A) Drone photomosaic of the North Loup River near Taylor, Nebraska, USA (Swanson et al., 2018). Brighter tan colors within the channel are subaqueous and represent higher portions of downstream-migrating bars beneath shallow water. Darker reaches of the channel represent deeper water. Mixed white and black areas with no crestlines mapped are subaerially exposed bar tops that are not currently undergoing fluvial transport. The location of panel B is shown in the black box. (B) Enlargement showing dune crestlines (short red lines) interpreted as perpendicular to dune transport direction. Black dashed arrows show general trends in local transport directions due to the steering of flow around bars. (C) Window length vs. the mean transport anomaly within the window. As the window length approaches that of the ~ 3 barforms or about half the reach, the sampled mean approaches the mean of the entire reach, indicating the total variability has been adequately sampled. Changes in curvature of this line are observed near multiples of mean bar length, supporting topographic steering as the source of the transport anomaly.

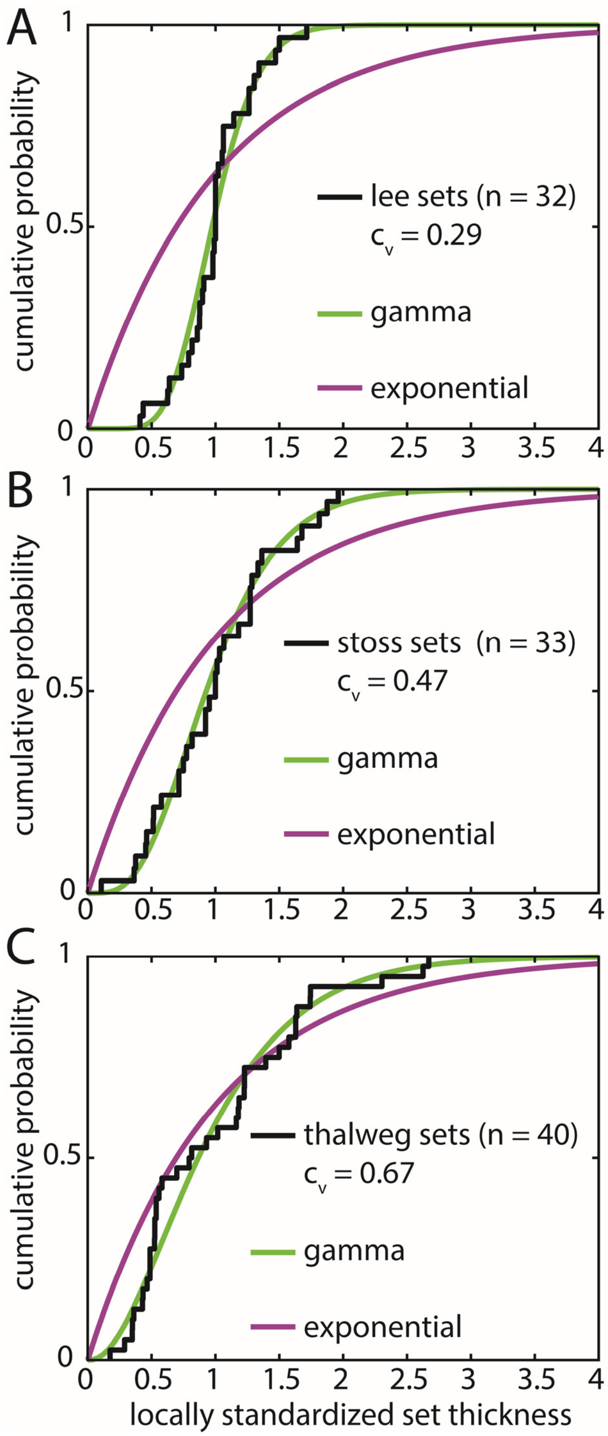

Figure 18 – (A) Cumulative distribution function (CDF) showing the mean- standardized distribution of set thickness located within bar lee environments (Fig. 14). (B) CDF of set thickness within bar stoss environments (Fig. 13). (C) CDF of thalweg set thickness (Fig. 15). The

best-fit gamma and exponential curves are shown for each distribution. In all cases, the exponential fits are rejected using a Kalmogorov-Smirnov test at a significance level of .05, and the gamma fits are not. This suggests all architectures required a significant rate of bed aggradation relative to the rate of dune migration, although the similarity of the two curves for thalweg sets indicates the ratio of bed aggradation to dune migration was the lowest of the three environments (Paola and Borgman, 1991; Jerolmack and Mohrig, 2005).

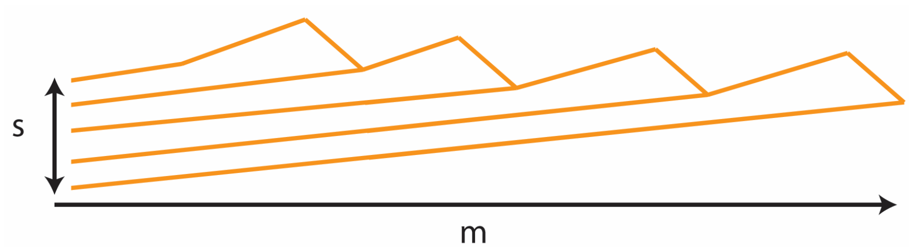

Figure 19 – A diagram explaining the calculation of accumulation time (Eq. 2). The relative rates of aggradation to migration are compared to deposit thickness, *s*, and and an assumed dune migration rate divided by the equivalent distance, *m*.

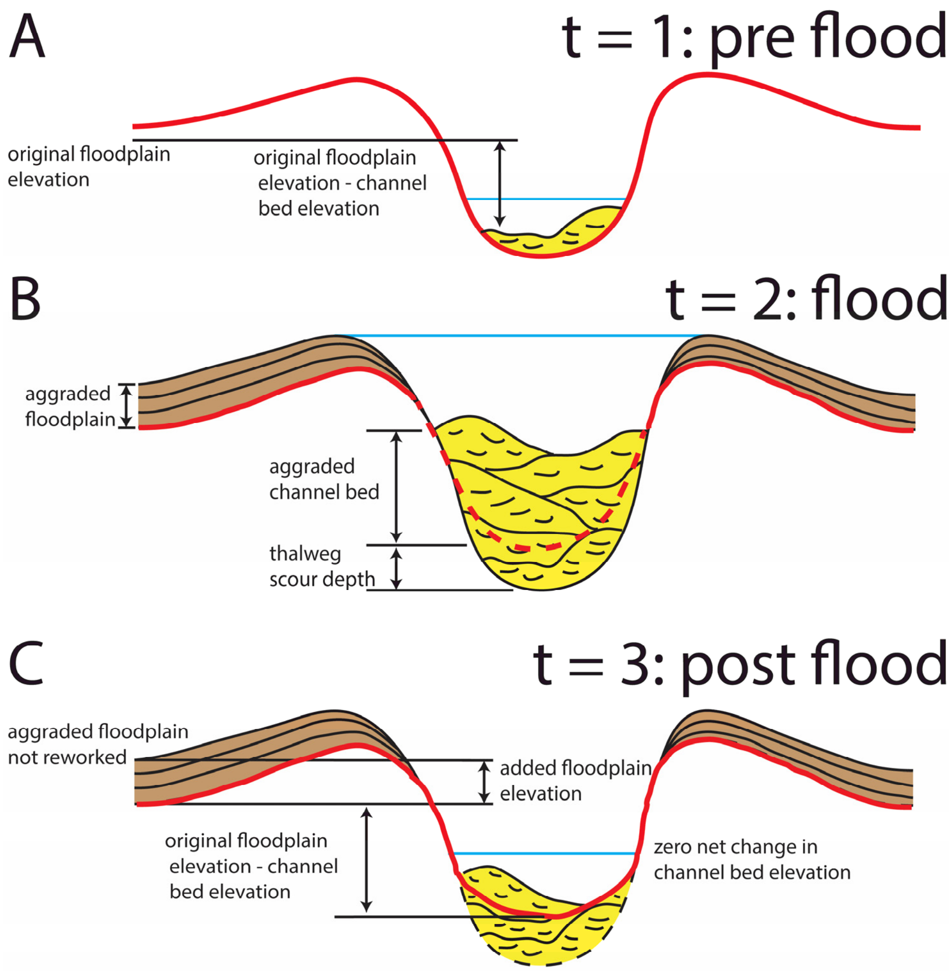

Figure 20 – A diagram merging the observations of the usually bypass-state channel bed and the relatively high amount of channel-bed aggradation preceding avulsion, when compared to other fluvial strata (e.g., Mohrig et al., 2000). (A) at t = 1, the distance between the lowest part of the floodplain and the channel bed (red line) during low flow is defined. (B) At t = 2, the channel is in flood stage. The floodplain has aggraded less than the channel bed. Avulsion does not occur. Original channel bed shown in red dashed line. (C) At t = 3, post-flood channel-bed reworking fills scours and removes accumulations such that there is zero net change in bed elevation.